

UNCLASSIFIED

AD NUMBER
ADB015193
NEW LIMITATION CHANGE
TO Approved for public release, distribution unlimited
FROM Distribution authorized to U.S. Gov't. agencies only; Test and Evaluation; Aug 1976. Other requests shall be referred to Air Force Armament Lab., Attn: DLDG, Eglin AFB, FL 32542.
AUTHORITY
3 Jul 1979 per Air Force Armament Lab/Armament Development and Test Ctr ltr

THIS PAGE IS UNCLASSIFIED

AFATL-TR-76-97 ✓

2

A SUMMARY OF SEVERAL PARAMETRIC INVESTIGATIONS OF THE EFFECT OF VARYING THE MATERIAL PROPERTIES OF A HEAVY METAL PENETRATOR

**SYSTEMS, SCIENCE AND SOFTWARE ✓
P. O. BOX 1620
LA JOLLA, CALIFORNIA 92038**

AUGUST 1976

FINAL REPORT: FEBRUARY - JUNE 1976

**D D C
RECEIVED
NOV 23 1976
ALBUQUERQUE**

**ADJ. N.J.
DDC FILE COPY.
ADBO15193**

Distribution limited to U. S. Government agencies only; this report documents test and evaluation; distribution limitation applied August 1976. Other requests for this document must be referred to the Air Force Armament Laboratory (DLG), Eglin Air Force Base, Florida 32542.

AIR FORCE ARMAMENT LABORATORY

AIR FORCE SYSTEMS COMMAND • UNITED STATES AIR FORCE

EGLIN AIR FORCE BASE, FLORIDA



COPY AVAILABLE TO DDC DOES NOT PERMIT FULLY LEGIBLE PRODUCTION

19 REPORT DOCUMENTATION PAGE		READ INSTRUCTIONS BEFORE COMPLETING FORM	
18 REPORT NUMBER AFATL-TR-76-97	2 GOVT ACCESSION NO.	3 RECIPIENT'S CATALOG NUMBER	
4 TITLE (and Subtitle) A SUMMARY OF SEVERAL PARAMETRIC INVESTIGATIONS OF THE EFFECT OF VARYING THE MATERIAL PROPERTIES OF A HEAVY METAL PENETRATOR.		5 TYPE OF REPORT OR PERIOD COVERED Final Report, 4 February 1976-31 June 1976	
6 AUTHOR(s) L. J. Hageman, R. T. Sedgwick J. L. Waddell		7 PROGRAMMING REPORT NUMBER SSS-R-76-2986	8 CONTRACT OR GRANT NUMBER(s) F08635-75-C-0844
9 MONITORING AGENCY NAME AND ADDRESS Systems, Science and Software P. O. Box 1620 La Jolla, California 92038		10 PROGRAM ELEMENT PROJECT TASK AREA & WORK UNIT NUMBERS Project No. 2560 Task No. Work Unit No. 332	
11 CONTROLLING OFFICE NAME AND ADDRESS Air Force Armament Laboratory Armament Development and Test Center Eglin Air Force Base, Florida		12 REPORT DATE August 1976	13 NUMBER OF PAGES 77
14 MONITORING AGENCY NAME & ADDRESS (if different from Controlling Office) 1277p.		15 SECURITY CLASS (of this report) Unclassified	
16 DISTRIBUTION STATEMENT (of this Report) Distribution limited to U. S. Government agencies only; this report documents test and evaluation; distribution limitation applied August 1976. Other requests for this document must be referred to the Air Force Armament Laboratory (DLDG), Eglin Air Force Base, Florida 32542.			
17 DISTRIBUTION STATEMENT (of the abstract entered in Block 20, if different from Report)			
18 SUPPLEMENTARY NOTES Available in the Defense Documentation Center (DDC).			
19 KEY WORDS (Continue on reverse side if necessary and identify by block number) Heavy Metal Penetrator Bulk Modulus HELP Normal Penetration Shear Modulus Yield Strength Numerical Techniques Spall Threshold Computer Simulation Eulerian Effects of Material Parameters			
20 ABSTRACT (Continue on reverse side if necessary and identify by block number) The two-dimensional HELP computer program was employed to augment two earlier parametric investigations involving the effects of varying the material properties of a heavy metal penetrator on the normal penetration of a 5.08-cm-thick steel plate. The projectile material properties that were varied were the shear yield strength, the tensile failure threshold, the shear modulus, and the bulk modulus. Conclusions were drawn from analysis of the			

REPRODUCTION QUALITY NOTICE

This document is the best quality available. The copy furnished to DTIC contained pages that may have the following quality problems:

- **Pages smaller or larger than normal.**
- **Pages with background color or light colored printing.**
- **Pages with small type or poor printing; and or**
- **Pages with continuous tone material or color photographs.**

Due to various output media available these conditions may or may not cause poor legibility in the microfiche or hardcopy output you receive.

If this block is checked, the copy furnished to DTIC contained pages with color printing, that when reproduced in Black and White, may change detail of the original copy.

UNCLASSIFIED

SECURITY CLASSIFICATION OF THIS PAGE(When Data Entered)

20. ABSTRACT (Concluded):

results from the current calculational effort as well as those from the two previous studies.

A tilted rectangular stamp or form with various fields and a large handwritten letter 'B' at the bottom left. The text within the stamp is partially legible and includes:

- SEARCHED
- SERIALIZED
- INDEXED
- FILED
- APR 1964
- FBI - MEMPHIS
- COMMUNICATIONS SECTION
- SEARCHED BY
- SERIALIZED BY
- INDEXED BY
- FILED BY

UNCLASSIFIED

SECURITY CLASSIFICATION OF THIS PAGE(When Data Entered)

PREFACE

This report documents the results of a study conducted by Systems, Science and Software, P. O. Box 1620, La Jolla, California 92038 under Contract No. F08635-75-C-0044 with the Air Force Armament Laboratory, Armament Development and Test Center, Eglin Air Force Base, Florida. Mr. Leonard L. Wilson (DLDG) managed the program for the Armament Laboratory. This effort was begun on 4 February 1976 and was completed on 30 June 1976.

This technical report has been reviewed and is approved for publication.

FOR THE COMMANDER:



GERALD P. D'ARCY, Colonel, USAF
Chief, Guns, Rockets and Explosives Division

TABLE OF CONTENTS

Section	Title	Page
I.	INTRODUCTION.	1
II.	NUMERICAL AND MATERIAL MODELS	3
	2.1 NUMERICAL TECHNIQUES	3
	2.2 MATERIAL MODEL	3
	2.2.1 Equation of State	5
	2.2.2 Elastic-Plastic Constitutive Relation and Yield Criterion.	5
	2.2.3 Failure in Tension.	6
	2.2.3.1 Dependence of Failure on Specific Internal Energy	6
	2.2.3.2 Gradual and Abrupt Failure Models	7
III.	DESCRIPTION OF THE PARAMETRIC STUDIES	9
IV.	EFFECTS OF CHANGES TO THE NUMERICAL MODEL AND COMPARISON WITH EXPERIMENT.	13
V.	RESULTS OF HELP CALCULATIONS.	16
	5.1 SUMMARY PLOTS AND TABLES	16
	5.2 EFFECTS OF VARYING THE PROJECTILE SHEAR STRENGTH	16
	5.3 EFFECTS OF VARYING THE TENSILE FAILURE THRESHOLD OF THE PROJECTILE.	29
	5.4 EFFECTS OF VARYING THE SHEAR MODULUS OF THE PROJECTILE.	34
	5.5 EFFECTS OF VARYING THE BULK MODULUS OF THE PROJECTILE.	41
VI.	CONCLUSIONS	46
	REFERENCES.	48
	APPENDIX A - PROJECTILE/TARGET CONFIGURATIONS AT VARIOUS TIMES FOR CALCULATIONS 1 THROUGH 19	49

LIST OF FIGURES

Figure	Title	Page
1.	Dimensions of the 30 mm Heavy Metal Penetrator Employed in the Material Parametric Studies.	10
2.	Crater Depth Versus Time for Calculations 1 and 18	15
3.	Projectile/Target Configuration at Various Times for Calculation 18	17
4.	Predicted Final Configurations of Calculations 12, 11, 13, 3, and 4.	21
5a.	Plot of Final Crater Radius Versus Projectile Shear Yield Strength for Calculations 3, 4, 11, 12, and 13.	22
5b.	Plot of Final Crater Depth Versus Projectile Shear Yield Strength for Calculations 3, 4, 11, 12, and 13.	22
6.	Plot of Final Projectile Length Versus Projectile Yield Strength for Calculations 3, 4, 11, 12, and 13.	24
7.	Crater Depth Versus Time for Calculations 3, 4, 11, 12, and 13.	25
8.	Total Energy Coupled to the Target Versus the Shear Yield Strength of the Projectile for Calculations 3, 4, 11, 12, and 13	27
9a.	Final Crater Profiles of Calculations 3 and 12	28
9b.	Final Crater Profiles of Calculations 3 and 4.	28
10.	Predicted Final Configurations of Calculations 6, 7, 19, and 18.	30
11.	Crater Depth Versus Time for Calculations 6 and 7 (Soft Projectiles)	31
12.	Crater Depth Versus Time for Calculations 18 and 19 (Hard Projectiles)	32

LIST OF FIGURES (Concluded)

Figure	Title	Page
13.	Final Crater Depth, Crater Radius and Length of Projectile Versus Spall Threshold for Calculations 6, 7, 18, and 19	33
14.	Plastic Work of Projectile and Total Energy Coupled to the Target for Calculations 6, 7, 19, and 19	35
15.	Configuration Plots of Calculations 6 and 19 at 160 μ s	36
16.	Final Configuration for Calculations 8, 14, 15, and 18.	38
17.	Crater Depth, Crater Radius and Total Energy Coupled to the Target Versus Time for Calculations 8, 14, 15, and 16.	39
18.	Final Projectile Length and Residual Projectile Kinetic Energy Versus Projectile Shear Modulus for Calculations 8, 14, 15, and 18.	40
19.	Crater Depth Versus Time for Calculations 8, 14, 15, and 18	42
20.	Predicted Final Configurations of Calculations 16, 17, and 18.	43
21.	Crater Depth, Crater Radius and Total Energy Coupled to Target for Calculations 16, 17, and 18	44
22.	Crater Depth Versus Time for Calculations 16, 17, and 18.	45

LIST OF TABLES

Table		Page
1.	Material Properties Employed in the Standard Calculation	4
2.	Projectile Material Properties Varied in Parametric Study	11
3.	Specific Calculations Used to Investigate Each of the Four Material Property Effects . . .	12
4.	Summary of Predicted Crater Dimensions and Projectile Length.	18
5.	Summary of Projectile Material Properties, Predicted Final Crater Dimensions, and Final Projectile Length Normalized to the Standard Calculation (18)	19
6.	Time of Crater Arrest and Total Energy Coupled to Target for Calculations 1 Through 19	20

SECTION I
INTRODUCTION

The mechanical properties of heavy metal alloys available for use as long rod kinetic energy penetrators vary over a wide range of values depending upon the constituents of the alloy and its heat treatment. The penetrator designer confronted with such choices of material properties must attempt to choose the particular alloy that will optimize penetrability. To accomplish this, he must understand the penetration process and how it is affected by penetrator configurational and material parameters.

Recently two theoretical investigations were undertaken for the purpose of aiding the designer in his choice of material properties for long rod penetration. In the first investigation (Reference 1) several heavy metal penetrators of different designs were ranked according to their penetrability when impacted against a 5.08-cm-thick steel target. In the second effort (Reference 2) one of the heavy metal penetrator designs was chosen and the effect of varying penetrator material properties was examined. In particular, calculations involving the variation in penetrator material yield strength, spall threshold, shear modulus, and bulk modulus were performed, and the effects of varying these properties on the projectile's ability to penetrate were investigated. The second effort led to several tentative conclusions regarding the dependency of final crater geometry on the various penetrator material properties.

The current effort was undertaken in order to substantiate or otherwise modify some of the earlier conclusions as well as to investigate ranges of parameters not considered in the previous investigations. In this report, data from the current effort are pooled with those generated in the previous investigations and the analyses reported here cover all of the data from all three of the efforts.

Section II of this report briefly describes the numerical and material models employed in the HELP calculations.

-
1. Sedgwick, R. T. and L. J. Walsh, "High Density Penetrator Performance in a Hard Target," AFATL-TR-74-201, ADB004857L, Air Force Armament Laboratory, Eglin Air Force Base, Florida, December 1974.
 2. Hageman, L. J. and R. T. Sedgwick, "A Parametric Investigation of the Effects of Varying the Material Properties of a Heavy Metal Penetrator," AFATL-TR-75-152, Air Force Armament Laboratory, Eglin Air Force Base, Florida, November 1975.

In Section III the parametric studies are summarized and the calculation matrix presented. Section IV discusses changes in the numerical model and validation of these changes by comparison with experimental data. In Section V the results from the calculations are presented and discussed. These results include plots which show the dependency of final crater depth and radius, final projectile length, and energy coupled to the target on such material properties as shear yield strength, failure threshold, shear modulus, and bulk modulus. Section VI presents the conclusions drawn from the combined current and previous investigations and provides recommendations for additional work.

The results from the combined parametric investigations of the effects of the material properties of heavy metal penetrators on the dimensions of the crater in a steel target indicate that available numerical techniques can provide invaluable guidance to the penetrator designer regarding the choice of penetrator material properties for a given penetrator design and given impact conditions.

SECTION II

NUMERICAL AND MATERIAL MODELS

2.1 NUMERICAL TECHNIQUES

In the present material parametric study of heavy metal penetrators, the HELP code was employed to solve a series of impact situations. In this section only a brief description of the numerical techniques and material models employed in the calculations is presented, since the HELP code is well documented (References 3 and 4).

HELP is a two-dimensional, multimaterial, Eulerian code for solving material flow problems in the hydrodynamic and elastic-plastic regimes. Although the code is basically Eulerian, material interfaces and free surfaces are propagated through the calculational mesh, in a Lagrangian manner, as discrete interfaces across which the materials are not allowed to interdiffuse. This interface treatment gives HELP a distinct advantage over other pure Eulerian codes and allows it to be applied to the solution of a variety of complex, multimaterial problems. The basic HELP techniques have been exercised over a wide range of solutions including hypervelocity and ballistic impact, fragmentation munitions, shaped charge jet formation and shaped charge jet penetration. Considerable confidence has been gained in the basic numerical model.

2.2 MATERIAL MODEL

The material model employed in HELP includes an equation of state, a deviatoric constitutive relation for elastic and plastic deformations, and a failure criterion. These will be discussed separately in the following paragraphs. The material constants used for the heavy metal projectile and for the steel target are given in Table 1.

-
3. Hageman, L. J. and J. M. Walsh, "HELP, A Multiple-Material Eulerian Program for Compressible Fluid and Elastic-Plastic Flows in Two Space Dimensions and Time," I and II, BRL-CR-39, AD Nos. 726459 and 7626460, Ballistic Research Laboratories, Aberdeen Proving Ground, Maryland, May 1971.
 4. Hageman, L. J., D. E. Wilkins, R. T. Sedgwick and J. L. Waddell, "HELP, A Multi-Material Eulerian Program for Compressible Fluid and Elastic-Plastic Flows in Two Space Dimensions and Time," Revised Edition, Systems, Science and Software Report SSS-R-75-2564, July 1975.

TABLE 1. MATERIAL PROPERTIES EMPLOYED
IN THE STANDARD CALCULATION

MATERIAL PROPERTY	HEAVY METAL ALLOY*	STEEL
ρ_0 (g/cm ³)	18.62	7.8
A (dynes/cm ²)	1.095×10^{12}	1.28×10^{12}
B (dynes/cm ²)	1.97×10^{12}	1.05×10^{12}
a	0.5	0.5
b	1.53	1.5
α	5.0	5.0
β	5.0	5.0
E_0 (ergs/g)	7.0×10^{10}	9.5×10^{10}
E_s (ergs/g)	6.73×10^9	2.44×10^{10}
E'_s (ergs/g)	2.37×10^{10}	1.02×10^{11}
G (dynes/cm ²)	7.75×10^{11}	8.0×10^{11}
Y_0 (dynes/cm ²)	1.01×10^{10}	6.0×10^9
Y_1 (dynes/cm ²)	0	0
Y_2 (dynes/cm ²)	0	0
E_m (ergs/g)	2.28×10^9	1.3×10^{10}
S (dynes/cm ²)	2.7×10^{10}	3.8×10^{10}

* Values of A, G, Y_0 , and S given in this table for the heavy metal alloy were employed in Calculations 1, 10, and 18. The values used in the remaining calculations are given in Table 2.

2.2.1 Equation of State

The Tillotson (Reference 5) equation of state, modified to give a smooth transition between condensed and expanded states, was employed. In Equations (1) through (3), p , E and ρ are pressure, specific internal energy and mass density, respectively; $\eta = \rho/\rho_0 = \mu + 1$, and ρ_0 , a , b , E_0 , E_s , E'_s , A , B , α and β are constants for the particular material. For the condensed states, i.e., when $\rho/\rho_0 > 1$, or for any cold states, $E < E_s$ the equation of state has the form

$$p = p_C = \left[a + \frac{b}{\frac{E}{E_0 \eta^2} + 1} \right] E \rho + A \mu + B \mu^2 \quad (1)$$

For expanded hot states, i.e., when $\rho/\rho_0 < 1$ and $E > E'_s$, the equation of state has the form

$$p = p_E = a E \rho + \left[\frac{b E \rho}{\frac{E}{E_0 \eta^2} + 1} + A \mu e^{-\beta(\rho_0/\rho - 1)} \right] e^{-\alpha(\rho_0/\rho - 1)^2} \quad (2)$$

A smooth transition between the condensed and expanded states is insured by a transition equation for the intermediate region defined by $E_s < E < E'_s$ and $\rho/\rho_0 < 1$. This blended portion of the equation of state has the form

$$p = \frac{(E - E_s)p_E + (E'_s - E)p_C}{E'_s - E_s} \quad (3)$$

2.2.2 Elastic-Plastic Constitutive Relation and Yield Criterion

The deviatoric stress increments, dS_{ij} , are determined by using the elastic relation

-
5. Tillotson, J. H., "Metallic Equations of State for Hyper-velocity Impact," General Atomic Report GA-3216, July 1962.

$$dS_{ij} = 2Gdc_{ij} \quad (4)$$

where G is the modulus of rigidity and dc_{ij} are the increments of deviatoric strain. When such an increment of stress causes the von Mises yield criterion,

$$s_{ij}s_{ij} \leq 2Y^2 \quad (5)$$

to be violated, each stress component is proportionately reduced to bring the stress normally back to the yield surface. A variable yield strength

$$Y = (Y_0 + Y_1\mu + Y_2\mu^2) (1 - E/E_m) \quad (6)$$

is defined to account for the increase in strength at high pressures and the decrease of strength at elevated values of the specific internal energy, E.

2.2.3 Failure in Tension

Given the spall threshold, S, based on plate slap experiments and expressed as a negative pressure, the maximum distension of a material is approximated in the HELP code by regarding the pressure as a linear function of the bulk modulus, ignoring higher order terms in ρ and any energy dependence. Therefore, given the spall threshold, S, and the bulk modulus A, the scalar quantity $(\rho/\rho_0)_s$ associated with the maximum distension of a material follows from

$$S = A \left((\rho/\rho_0)_s - 1 \right) \quad (7)$$

i.e.,

$$(\rho/\rho_0)_s = \frac{S}{A} + 1 \quad (8)$$

2.2.3.1 Dependence of Failure on Specific Internal Energy

Previous to these three studies, the material failure criterion in HELP was based solely on material distension as

indicated by the scalar quantity $(\rho/\rho_0)_s$. However, in the present parametric studies, this criterion was extended to account for the effect of heating on the material's ability to withstand tension. It was assumed that the spall threshold approached zero as the material's specific internal energy approached E_{melt} , the energy needed to melt the material.

The density corresponding to the melt state, ρ_{melt} , was determined such that

$$P(\rho_{melt}, E_{melt}) = 0. \quad (9)$$

If the material was between the cold and melt states, then

$$(\rho/\rho_0)_s = \left(\frac{S}{A} + 1\right) + \frac{E}{E_{melt}} \left[\frac{\rho_{melt}}{\rho_0} - \left(\frac{S}{A} + 1\right) \right] \quad (10)$$

which is a straight-line interpolation in the $E - \rho$ plane between the values associated with the cold and melt states.

2.2.3.2 Gradual and Abrupt Failure Models

When the distension, ρ/ρ_0 , of the material in a computational cell was less than $(\rho/\rho_0)_s$, the material was presumed to have failed. In all but one of the calculations in these studies, the material was failed gradually over a characteristic time. The characteristic time was determined for each cell by dividing the cell diagonal by the sound speed of the material. The material in a cell had to be subjected to conditions that would cause failure for a time duration equal to the characteristic time in order for the material in that cell to be completely failed. If the stress conditions changed before the cell completely failed, the material was considered only partially damaged. In order to keep track of this damage, a failure array, F_k , was added to the code. When $F_k = 0$, the material in the k th cell had not failed, and when $F_k = 1$, it had completely failed. Intermediate values of F would be associated with cells which had satisfied the failure criterion for a time duration less than the characteristic time. The total stresses calculated in each damaged cell were reduced by the factor $(1 - F)$.

In the abrupt failure model employed in Calculation 10, the value of F was set immediately to 1 once the material was subjected to conditions which violated the failure criterion.

In both the gradual and abrupt failure models, the failure parameter, F, was transported so as to associate it with a volume of material rather than with a fixed computational cell. Therefore, values of F between 0 and 1 could result from material that was gradually failing over a characteristic time when the gradual failure model was employed, or from failed material being transported when either model was employed.

SECTION III

DESCRIPTION OF THE PARAMETRIC STUDIES

The HELP calculations performed in the two previous investigations and in the current parametric study involved the normal penetration of a heavy metal projectile into 5.08-cm-thick rolled homogeneous armor (RHA) at a velocity of 5.5×10^4 cm/sec. The material properties and design of the penetrator in Calculation 1 of the first study was chosen as the standard for the subsequent material property parametric studies. The material properties of the projectile in Calculation 1 were chosen as being representative of a real heavy metal alloy. The dimensions of the projectile are given in Figure 1. The material properties of the steel target were held constant throughout the studies. (The material constants used for the standard projectile and the steel target are given in Table 1.)

In this report the results of the calculations from the second study were combined with those of the current investigation so that firmer conclusions regarding the effects of penetrator material properties on the penetration process could be made. Table 2 provides the calculational matrix. Most of the calculations shown in Table 2 involved variations from the standard values assigned to the spall threshold, shear yield strength, bulk modulus, and rigidity modulus in Calculation 1. Two of the calculations, numbers 10 and 18, were performed to assess the effects of specific numerical techniques: abrupt failure and the addition of an artificial viscosity term to cell boundary stresses. An analysis of the results of Calculations 10 and 18 is given in Section IV of this report. It should be noted here, however, that the results of those calculations indicated that Calculations 1 and 2 should be omitted from the material property parametric study and that Calculation 18 should become the standard in place of Calculation 1.

Table 3 indicates the specific calculations which were chosen for investigating the effects of varying each of the four material properties. These effects are discussed in detail in Section V.

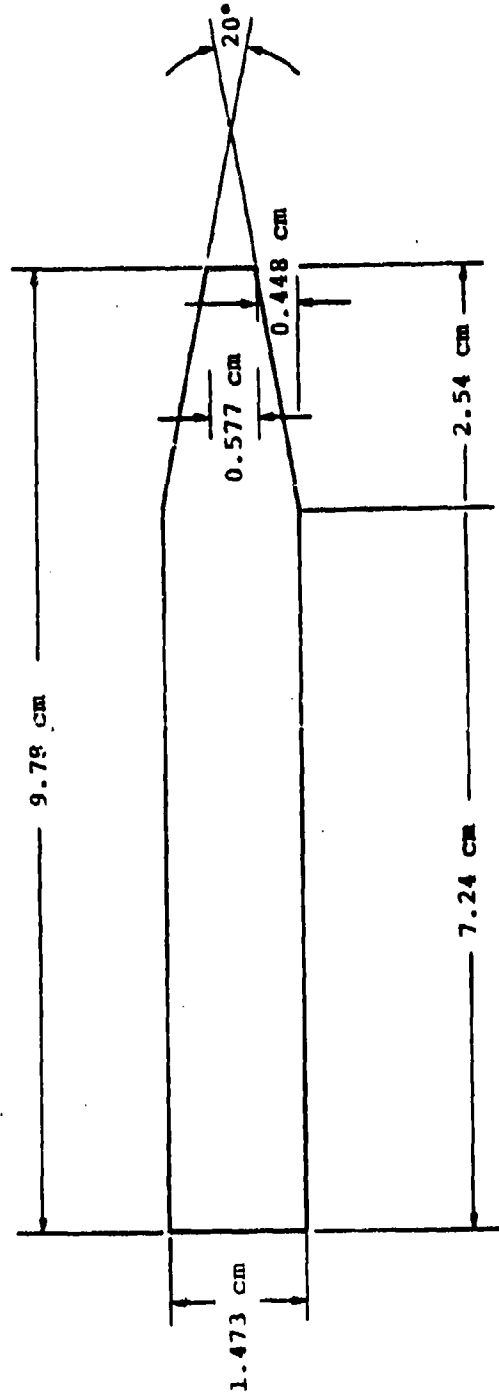


Figure 1. Dimensions of the 30 mm Heavy Metal Penetrator Employed in the Material Parametric Studies

TABLE 2. PROJECTILE MATERIAL PROPERTIES VARIED IN PARAMETRIC STUDY

Calculation Number	Shear field τ_0 (dynes/cm ² x 10 ⁹)	Shear Modulus G (dynes/cm ² x 10 ¹¹)	Spall Threshold S (dynes/cm ² x 10 ⁹)	Pulk Modulus A (dynes/cm ² x 10 ¹²)
First Study (1974)				
1*	10.10	7.75	27	1.095
2*	3.59	7.02	35	1.095
3	7.56	7.75	36	1.095
4	15.10	7.75	36	1.095
5	5.04	7.75	12	1.095
6	3.78	7.75	18	1.095
7	3.78	7.75	27	1.095
8	10.10	15.50	27	1.095
9	10.10	7.75	27	2.190
10**	10.10	7.75	27	1.095
11	1.51	7.75	36	1.095
12	9.75	7.75	36	1.095
13	2.55	7.75	36	1.095
14	10.10	31.00	27	1.095
15	10.10	3.875	27	1.095
16***	10.10	7.75	14.7	0.5975
17***	10.10	7.75	108	4.38
18	10.10	7.75	27	1.095
19	10.10	7.75	18	1.095

* Artificial Viscosity Added to Cell Boundary Stresses

** Abrupt Failure Model Employed

*** (ρ/ρ_0) Held Constant and Equal to That of Calculation 18

TABLE 3. SPECIFIC CALCULATIONS USED TO INVESTIGATE EACH OF THE FOUR MATERIAL PROPERTY EFFECTS

MATERIAL PROPERTY	CALCULATION NUMBERS
Shear Yield, Y_0	3, 4, 11, 12, 13
Spall Threshold, S	6, 7, 18, 19
Shear Modulus, G	8, 14, 15, 18
Bulk Modulus, A	16, 17, 18

SECTION IV
EFFECTS OF CHANGES TO THE NUMERICAL MODEL AND
COMPARISON WITH EXPERIMENT

In the first study (Reference 1), the design which was chosen for Calculation 1 was tested experimentally and the resulting crater dimensions were compared to those predicted by the HELP code. The discrepancy of 10 percent was somewhat surprising since the results of the HELP code in other impact studies had been significantly closer to experimental results (References 6 through 8). In reviewing the precise model used in that first study (Calculations 1 and 2), it was concluded that the addition of an artificial viscosity term in the form of a cell boundary stress was not only unnecessary, but it was probable that by smearing the stress field the added viscosity had significantly reduced the interface velocity and the predicted final crater depth. The addition of an artificial viscosity term was based on studies made on a very brittle material in which small noises in the stress field led to unrealistic propagation of failure. Initially, it was thought that such unrealistic failure might occur in the heavy metal penetrator even though it was relatively ductile. In the subsequent studies, however, the additional artificial viscosity term was omitted from most of the calculations, and no evidence of unrealistic failure propagation was observed.

In the current study the first calculation was repeated; it is reported here as Calculation 18. The crater depth of Calculation 1 (with viscosity) was 1.382 cm, whereas the

-
6. Sedgwick, R. T., and L. J. Hageman, "Numerical, Analytical and Experimental Investigation of Penetration by Kinetic Kinetic Energy Projectiles," AFATL-TR-72-48, March 1972.
 7. Sedgwick, R. T., M. S. Chawla and L. J. Walsh, "Parametric Application of Computer Codes to Metallic Projectile/Target Interactions," Systems, Science and Software Final Report SSS-R-73-1631 under Contract F08635-71-C-0094, April 1973.
 8. Sedgwick, R. T., and J. M. Walsh, "Effects of Projectile Shape on Thin Plate Perforation at Normal Incidence," BRL-CR-38, May 1971.

crater depth of Calculation 18 (without viscosity) was 1.53 cm, an increase of 10.7 percent which brings the calculated results within a percent of the experimental results. Crater depth as a function of time is plotted for Calculations 1 and 18 in Figure 2. As these curves indicate, the crater formation process is nearly identical in the two calculations for the first 50 μ s after impact. From then on, however, the added artificial viscosity in Calculation 1 significantly reduces the rate of crater growth and the final crater depth.

Because of its close agreement with experiment, Calculation 18 becomes, in this current study, the basic calculation in place of Calculation 1. Calculation 2 is omitted from the comparisons in this report since it also was part of the first study and reflects the use of an additional artificial viscosity term. Furthermore, the rigidity modulus used in Calculation 2 was 10 percent lower than that used in Calculations 6 and 7, thereby making the previous conclusions on the effect of varying the shear yield strength unnecessarily tentative.

In the second study an additional artificial viscosity term was employed in Calculation 9 in which the projectile material bulk modulus was twice the standard value. In view of the above observations on the effects of this added viscosity, Calculation 9 is omitted from the current analysis of the effects of varying the projectile material bulk modulus.

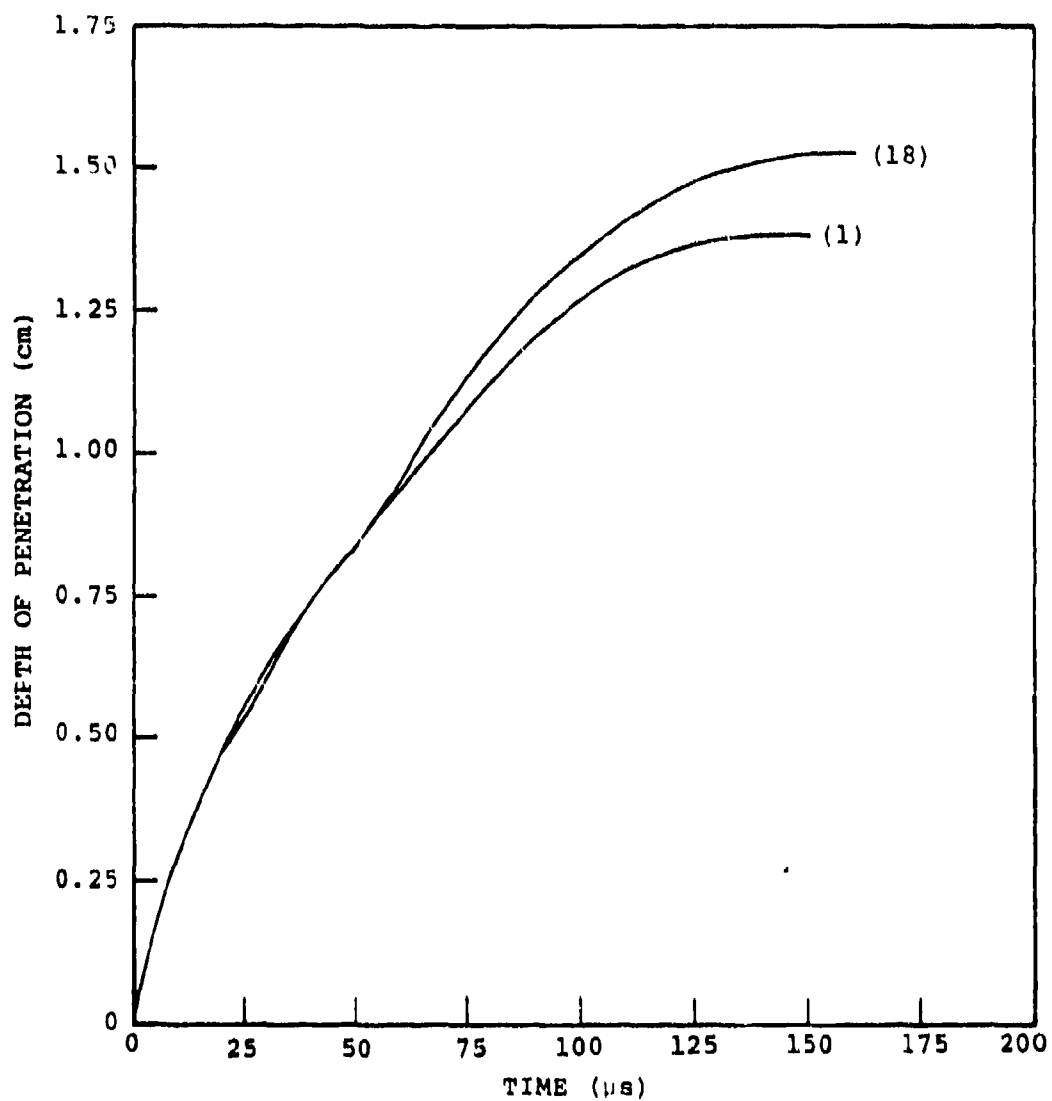


Figure 2. Crater Depth Versus Time for Calculations 1 and 18

SECTION V

RESULTS OF HELP CALCULATIONS

5.1 SUMMARY PLOTS AND TABLES

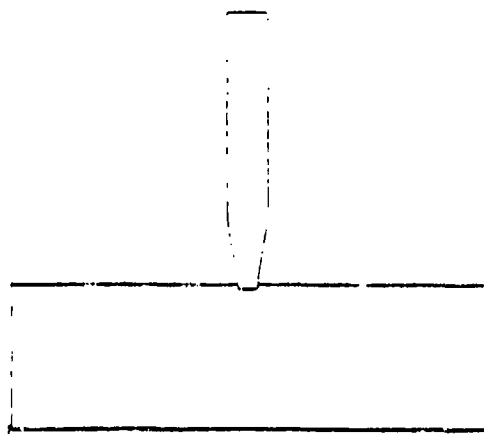
The HELP calculations reported here followed the penetration process until the depth of the crater became constant. The effectiveness of each projectile material modeled is measured primarily in terms of the final crater depth. The values of crater radius and projectile length at that final time as well as the total energy coupled to the target are presented as indicators of differences in the penetration process and are not meant to represent the ultimate values of these parameters which may continue to change after the final crater depth has been established.

To illustrate the intermediate stages of the penetration process, plots of the projectile/target configurations at various times for the standard calculation (number 18 in Table 2) are shown in Figure 3. (The configuration plots for all nineteen HELP calculations as well as the grid zoning employed in all of the calculations are presented in Appendix A.)

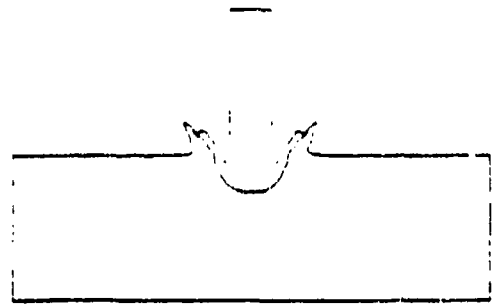
The results of the nineteen calculations are summarized in Tables 4, 5, and 6. Table 4 lists the quantitative predictions regarding the final crater depth and the corresponding crater radius and projectile length. Table 5 normalizes these quantities to Calculation 18, the basic case in the parametric study. Table 6 indicates the final time for each calculation (i.e., the time at which the final crater depth was established) and the total energy coupled to the target from the time of impact to the final time.

5.2 EFFECTS OF VARYING THE PROJECTILE SHEAR STRENGTH

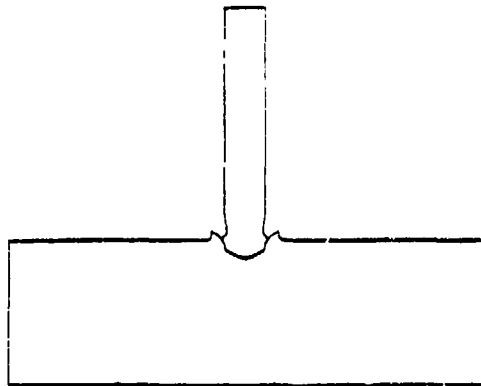
The effects of increasing the shear yield strength of the projectile, as predicted by the HELP calculations, can be seen by comparing the results of Calculations 12, 11, 13, 3 and 4 in which the projectile yield strength was 0.75, 1.51, 2.55, 7.56, and 15.1 kilobars, respectively. The final configurations of these calculations are given in Figure 4. It is clear from these configuration plots that the hardness of the projectile material significantly affects the final depth and shape of the crater. From the curves drawn through the data points in Figure 5, it is apparent that, as the shear yield strength of the projectile is increased, the crater radius decreases almost linearly, whereas the crater depth is essentially unaffected by increasing the projectile shear



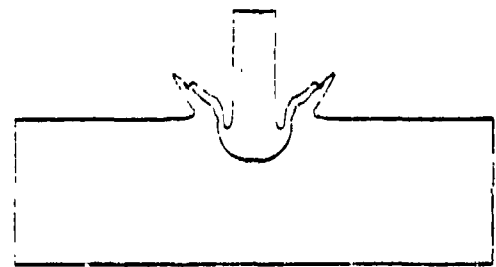
$t = 5 \mu s$



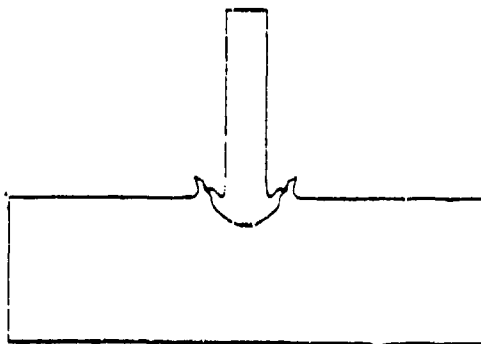
$t = 90 \mu s$



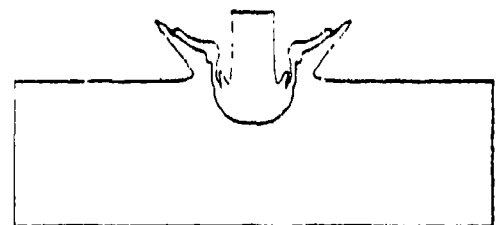
$t = 30 \mu s$



$t = 120 \mu s$



$t = 60 \mu s$



$t = 160 \mu s$

Figure 3. Projectile/Target Configuration at Various Times for Calculation 18. ($S = 2.7 \times 10^{10}$, $Y_0 = 1.01 \times 10^{10}$, $G = 7.75 \times 10^{11}$, $A = 1.095 \times 10^{12}$)

TABLE 4. SUMMARY OF PREDICTED CRATER DIMENSIONS AND PROJECTILE LENGTH

Calculation Number	Shear Yield γ_c (dynes/cm ² × 10 ⁹)	Shear Modulus G (dynes/cm ² × 10 ¹¹)	Spall Threshold S (dynes/cm ² × 10 ⁹)	Bulk Modulus K (dynes/cm ² × 10 ¹²)	Final Crater Depth (on axis) (cm)	Final Crater Radius (cm)	Final Projectile Length (cm)
1	10.10	7.75	27	1.095	1.382	1.520	4.368
2	3.59	7.02	36	1.095	1.094	2.081	2.814
3	7.56	7.75	36	1.095	1.536	1.523	3.432
4	15.10	7.75	36	1.095	1.764	1.324	4.19
5	5.04	7.75	12	1.095	1.822	1.542	1.666
6	3.78	7.75	18	1.095	2.226	1.572	0.808
7	3.78	7.75	27	1.095	1.472	1.744	1.388
8	10.10	15.50	27	1.095	1.654	1.524	3.050
9	10.10	7.75	27	2.190	1.296	1.477	4.248
10	10.10	7.75	27	1.095	1.254	1.472	4.286
11	1.51	7.75	36	1.095	1.36	1.785	1.232
12	0.75	7.75	36	1.095	1.500	1.819	1.190
13	2.55	7.75	36	1.095	1.417	1.63	1.526
14	16.10	31.00	27	1.095	1.582	1.57	3.242
15	10.10	3.875	27	1.095	1.702	1.45	4.036
16	10.10	7.75	14.7	0.5975	1.654	1.459	2.918
17	10.10	7.75	108.2	4.38	1.699	1.524	3.294
18	16.10	7.75	27	1.095	1.530	1.511	3.868
19	10.10	7.75	18	1.095	1.541	1.509	3.830

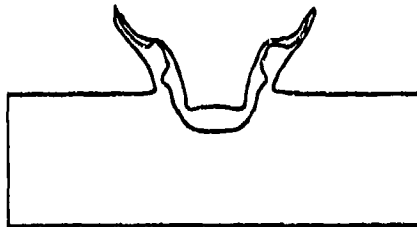
TABLE 5. SUMMARY OF PROJECTILE MATERIAL PROPERTIES, PREDICTED FINAL CRATER DIMENSIONS, AND FINAL PROJECTILE LENGTH NORMALIZED TO THE STANDARD CALCULATION (18)

Calculation Number	Normalized Shear Yield Strength σ_y	Normalized Shear Modulus G	Normalized Spall Threshold S	Normalized Bulk Modulus A	Normalized Crater Depth	Normalized Crater Radius	Normalized Final Projectile Length
18	1.000	1.000	1.000	1.000	1.000	1.000	1.000
1	1.000	1.000	1.000	1.000	0.903	1.006	1.129
2	0.355	0.906	1.333	1.000	0.715	1.577	0.728
3	0.749	1.000	1.333	1.000	0.873	1.008	0.887
4	1.495	1.000	1.333	1.000	1.153	0.876	1.083
5	0.499	1.000	0.444	1.000	1.191	1.021	0.431
6	0.374	1.000	0.667	1.000	1.455	1.040	0.209
7	0.374	1.000	1.000	1.000	0.962	1.154	0.359
8	1.000	2.000	1.000	1.000	1.081	1.009	0.789
9	1.000	1.000	1.000	2.000	0.847	0.977	1.098
10	1.000	1.000	1.000	1.000	0.820	0.974	1.108
11	0.150	1.000	1.333	1.000	0.889	1.181	0.243
12	0.074	1.000	1.333	1.000	0.980	1.204	0.308
13	0.252	1.000	1.333	1.000	0.926	1.079	0.395
14	1.000	4.000	1.000	1.000	1.034	1.039	0.838
15	1.000	0.500	1.000	1.000	1.112	0.960	1.043
16	1.000	1.000	0.547	0.546	1.081	0.966	0.754
17	1.000	2.000	4.007	4.000	1.111	1.019	0.852
19	1.000	1.000	0.667	1.000	1.007	0.999	0.990

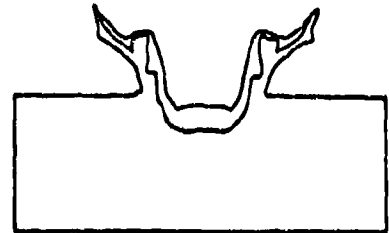
TABLE 6. TIME OF CRATER ARREST AND TOTAL ENERGY COUPLED TO TARGET FOR CALCULATIONS 1 THROUGH 19

CALCULATION NUMBER	TIME OF CRATER ARREST (μ s)	TOTAL ENERGY COUPLED TO TARGET (ergs $\times 10^{11}$)
1	150	1.486
2	160	1.261
3	160	1.415
4	200	1.619
5	210	1.943
6	235	2.607
7	220	1.764
8	200	1.637
9	150	1.356
10	150	1.315
11	200	1.793
12	205	1.930
13	190	1.645
14	210	1.536
15	160	1.629
16	210	1.516
17	220	1.567
18	160	1.502
19	160	1.544

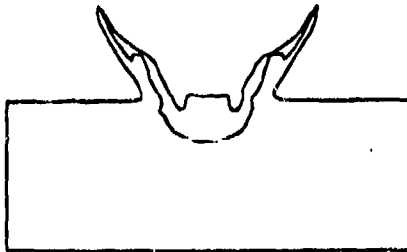
Calculation 12
 $Y_0 = 0.75 \text{ kb}$



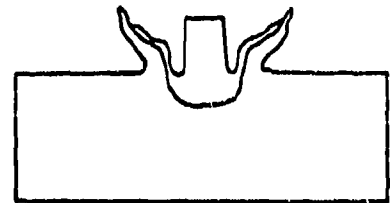
Calculation 11
 $Y_0 = 1.51 \text{ kb}$



Calculation 13
 $Y_0 = 2.55 \text{ kb}$



Calculation 3
 $Y_0 = 7.56 \text{ kb}$



Calculation 4
 $Y_0 = 15.1 \text{ kb}$

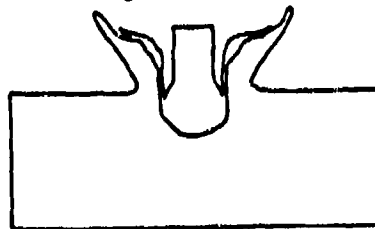


Figure 4. Predicted Final Configurations of Calculations 12, 11, 13, 3, and 4

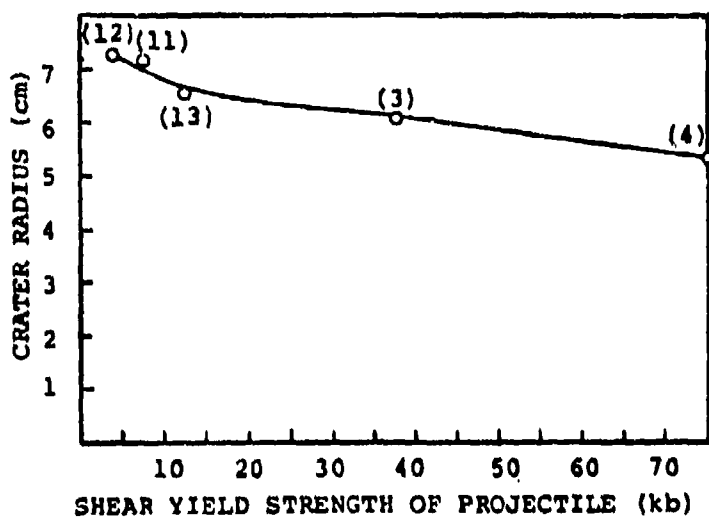


Figure 5a. Plot of Final Crater Radius Versus Projectile Shear Yield Strength for Calculations 3, 4, 11, 12 and 13

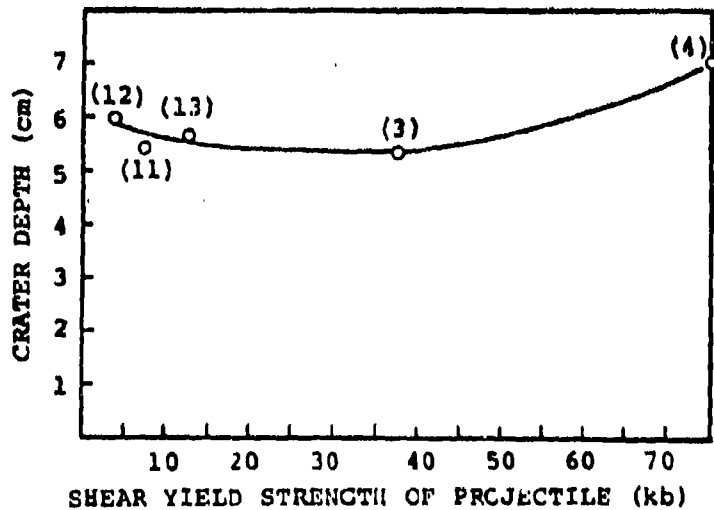


Figure 5b. Plot of Final Crater Depth Versus Projectile Shear Yield Strength for Calculations 3, 4, 11, 12 and 13

yield strength from 0.75 to 7.56 kilobars and is increased by 24 percent when the projectile shear yield strength is increased from 7.56 to 15.1 kilobars.

The second parameteric investigation of heavy metal penetrators predicted a minimum in the crater depth versus projectile shear yield strength curve corresponding to the results of Calculation 2. The additional calculations completed as part of the present study (numbers 12 and 13) indicate a slight upturn in the curve at very low values of the projectile shear yield strength. However, by excluding the results of Calculation 2 from the present analysis, the importance and magnitude of the minimum point are greatly diminished.

Additional data extracted from these HELP calculations suggest a rather abrupt change in the extent of projectile deformation as the projectile yield strength is raised above 7 kilobars. It is already clear from the configuration plots in Figure 4 that the hardness of the projectile significantly affects how much of the projectile mass becomes part of the ejecta and how much remains essentially undeformed. In Figure 6 the curve showing the relationship between projectile hardness and final projectile length drops off abruptly between yield strengths of 7.56 and 2.55 kilobars. Outside of this range, however, the slope of the curve predicts a much weaker dependence of final projectile length on projectile hardness. There appears to be a relatively narrow range of values for projectile shear yield strength (between 2.55 and 7.56 kilobars in the impact situation modeled by these calculations) which defines a transition between the projectile materials in which all or most of the projectile mass becomes part of the ejecta and those in which a significant portion of the back of the projectile remains essentially undeformed. This critical range of values probably is a function of the impact velocity, the material properties of the target, and the other material properties of the projectile. For example, a lower tensile failure threshold in the projectile or a higher yield strength in the target might cause this transition to occur at higher values of projectile yield strength.

A basic difference in the cratering process due to the use of hard rather than soft projectile materials also is indicated by the crater depth versus time curves in Figure 7. When the harder projectile materials ($Y_0 > 7.56$ kb) are used, Calculations 3 and 4 predict that the final crater depth is established earlier and more abruptly than when the softer materials ($Y_0 \leq 2.55$ kb) are chosen, as in Calculations 11, 12, and 13. By taking the first derivative of these curves, the velocity of the projectile/target interface can be obtained. Figure 7 therefore indicates that in Calculations 3 and 4 the

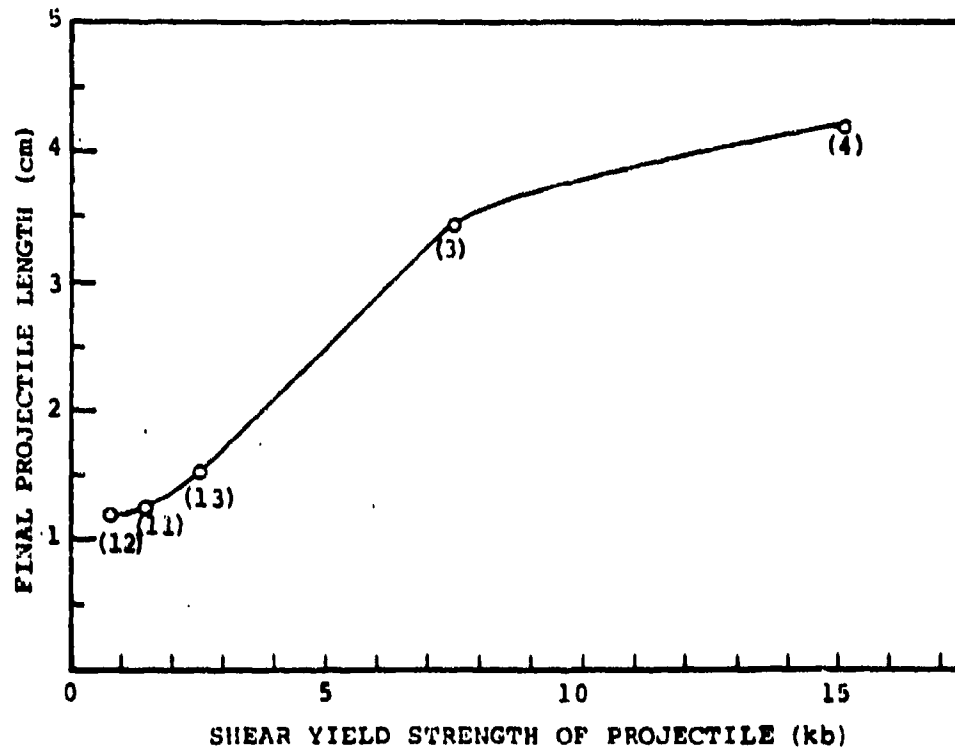


Figure 6. Plot of Final Projectile Length Versus Projectile Yield Strength for Calculations 3, 4, 11, 12, and 13

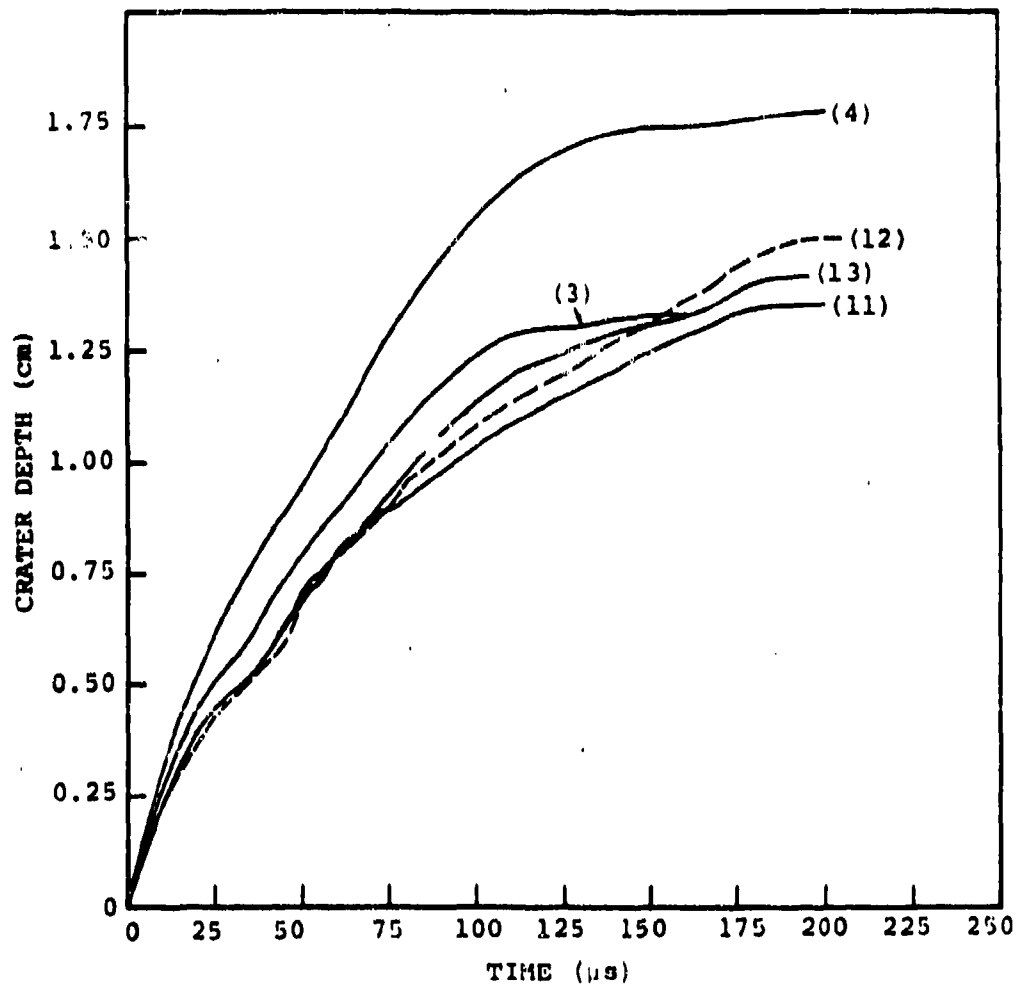


Figure 7. Crater Depth Versus Time for Calculations 3, 4, 11, 12, and 13

interface velocity remains nearly constant until about 100 μ s and then over the next 40 μ s quickly approaches zero. By contrast, in Calculations 11 and 12, where $Y_0 < 1.51$ kb, the interface velocity drops off very slowly for 175 μ s and goes to zero only when the residual length of the projectile approaches zero (as seen in Figure 4). Calculation 13, in which $Y_0 = 2.55$ kbar, represents a transition between the extremes. The deceleration of the projectile/target interface occurs more rapidly, as it does when the hard materials are employed, but the interface continues to move until most of the projectile material has been consumed, which is characteristic of the softer materials.

This difference in crater growth rate and in residual projectile length suggest that when the yield strength is sufficiently high (> 7.56 kb), the projectile is stopped by stresses within the projectile as well as by those within the target. Furthermore, when the yield strength of the projectile material is sufficiently low (< 1.51 kb), these stresses are not sufficient to stop the projectile until it is entirely consumed by the cratering process.

A difference in the effect of the hard and soft projectile materials is reflected also by Figure 8 in which the total energy coupled to the target is plotted versus projectile shear yield strength. The softer projectiles ($Y_0 \leq 2.55$ kb), which form wider craters and thereby distribute their load over a larger surface area, couple more total energy to the target than do the harder projectiles ($Y_0 > 7.56$ kb). These results are not surprising in light of the fact that more of the hard projectile's kinetic energy is converted to heat by plastic work and therefore less of it is available to be coupled to the target. In addition, the hard projectile, because it flows less radially, focuses its load over a smaller surface area and thereby forms a deeper, narrow crater even though it couples less total energy to the target. The crater profiles in Figure 9 show the change in crater shape as the yield strength of the projectile material is increased.

To summarize, the results from Calculations 3 and 4 predict a 24 percent gain in crater depth when the projectile material shear yield strength is increased by a factor of two from 7.56 to 15.1 kilobars. However, when this parameter is increased from 0.75 to 7.56 kilobars, a factor of ten, Calculations 12 and 3 predict narrower but not deeper craters. Crater depth, therefore, has a nonlinear dependence on projectile hardness over the range of values considered here (0.75 to 15.1 kb). Furthermore, above a critical value of projectile yield strength, the cratering process apparently changes

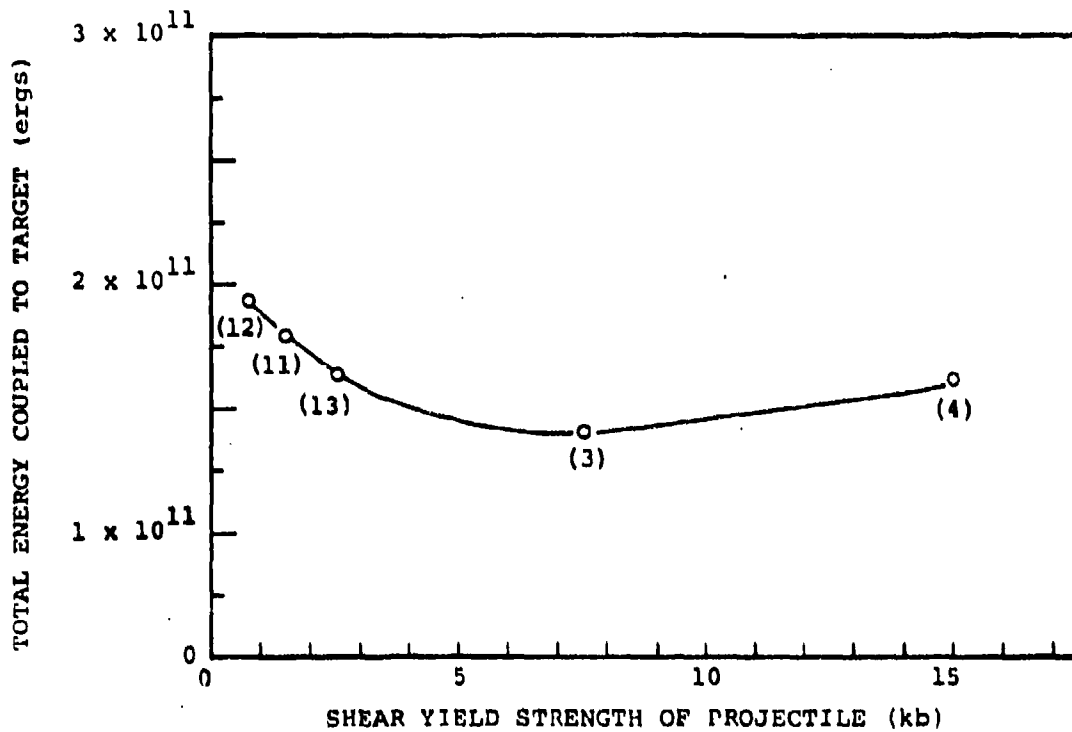


Figure 8. Total Energy Coupled to the Target Versus the Shear Yield Strength of the Projectile for Calculations 3, 4, 11, 12, and 13

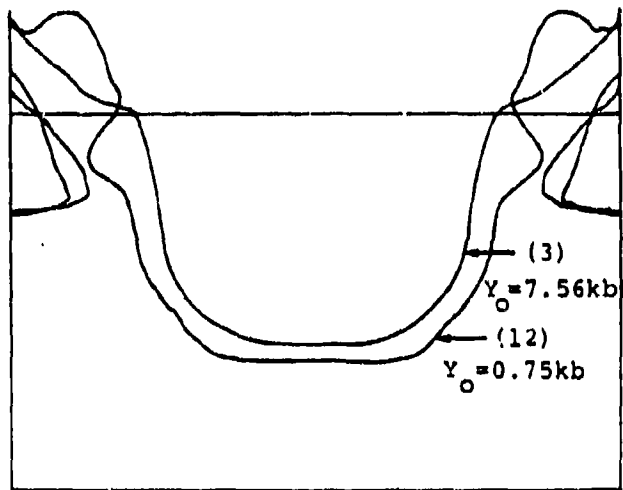


Figure 9a. Final Crater Profiles of Calculations 3 and 12

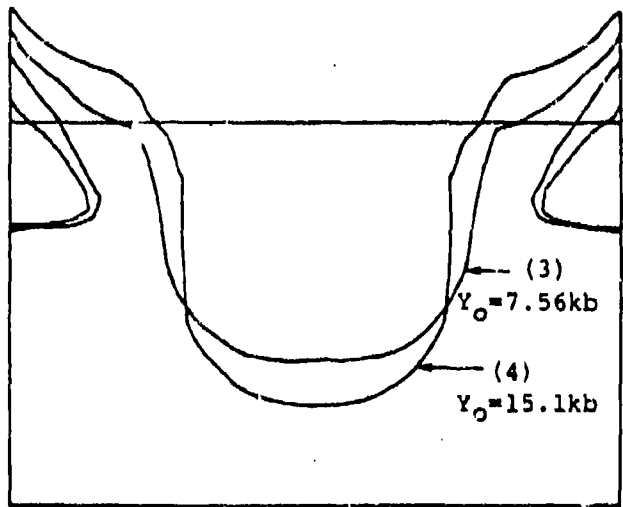


Figure 9b. Final Crater Profiles of Calculations 3 and 4

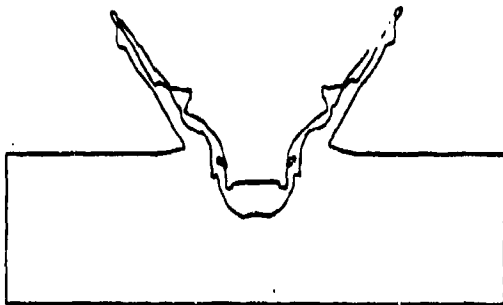
character; i.e., the residual projectile length increases rapidly, the growth of the crater ends abruptly, and before all of the projectile is consumed. This critical value is very probably a function of the impact velocity, the target material properties, the other projectile material properties, and the initial dimensions of the projectile.

5.3 EFFECTS OF VARYING THE TENSILE FAILURE THRESHOLD OF THE PROJECTILE

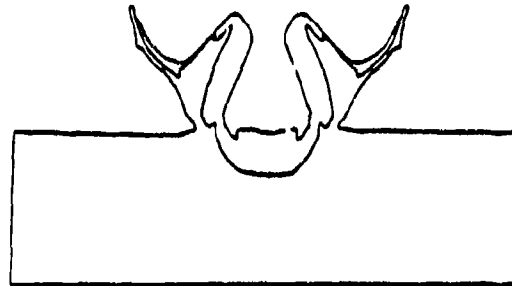
The effects of changing the tensile failure threshold of the projectile can be seen by comparing the results of Calculations 6 and 7 and those of Calculations 18 and 19. As indicated in Table 2, the projectiles in Calculations 6 and 7 were relatively soft, having a yield strength of 3.78 kilobars, whereas the projectiles in Calculations 18 and 19 had a yield strength of 10.1 kilobars, representing a relatively hard material. In both sets the spall threshold of one was 27 kilobars (Calculations 7 and 18), and the other was 18 kilobars (Calculations 6 and 19).

The failure criterion employed in these calculations is described in Section II. However, a brief description of how the criterion is applied seems appropriate at this point. When the material in a calculational cell satisfies the failure criterion over a characteristic time, the code presumes that the material has become a collection of small particles which is unable to withstand tension (negative pressure) and has no strength in shear. However, the code does assume that this failed material can later sustain hydrostatic pressures if it becomes sufficiently compressed or heated.

As the configuration plots and the crater depth versus time plots in Figures 10 through 12 indicate, varying the tensile threshold of a soft projectile ($Y_0 = 3.78$ kb) has a significant effect on the final crater geometry; whereas, this parameter when varied from 18 to 27 kilobars in a hard penetrator material ($Y_0 = 10.1$ kb) has essentially no effect on the final crater dimensions or on the penetration process. These conclusions are summarized by Figures 13a, 13b, and 13c in which final crater depth, crater radius, and projectile length are plotted versus the projectile spall threshold for Calculations 6 and 7 and Calculations 18 and 19. For the hard projectiles (18 and 19) all of these quantities are essentially the same. For the soft projectiles (6 and 7), however, crater depth is clearly affected by changes in the tensile failure of the projectile; the crater radius and the final length of the projectile are also affected but to a lesser degree. In fact, the final length of the projectile is more sensitive to projectile yield strength than it is to spall threshold as is evidenced by the spread in the data for the soft and hard projectiles in Figure 13c.

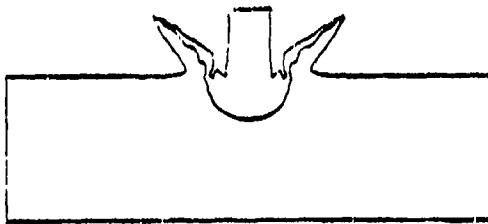


Calculation 6
S = 18 kb

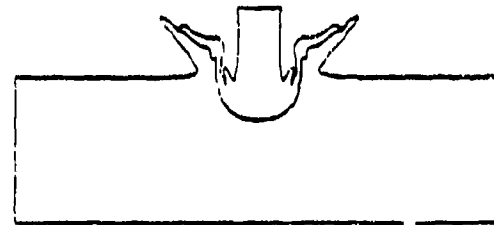


Calculation 7
S = 27 kb

$Y_0 = 3.78 \text{ kb}$



Calculation 19
S = 18 kb



Calculation 18
S = 27 kb

$Y_0 = 10.1 \text{ kb}$

Figure 10. Predicted Fin - Configurations of Calculations 6, 7, 19 and 18

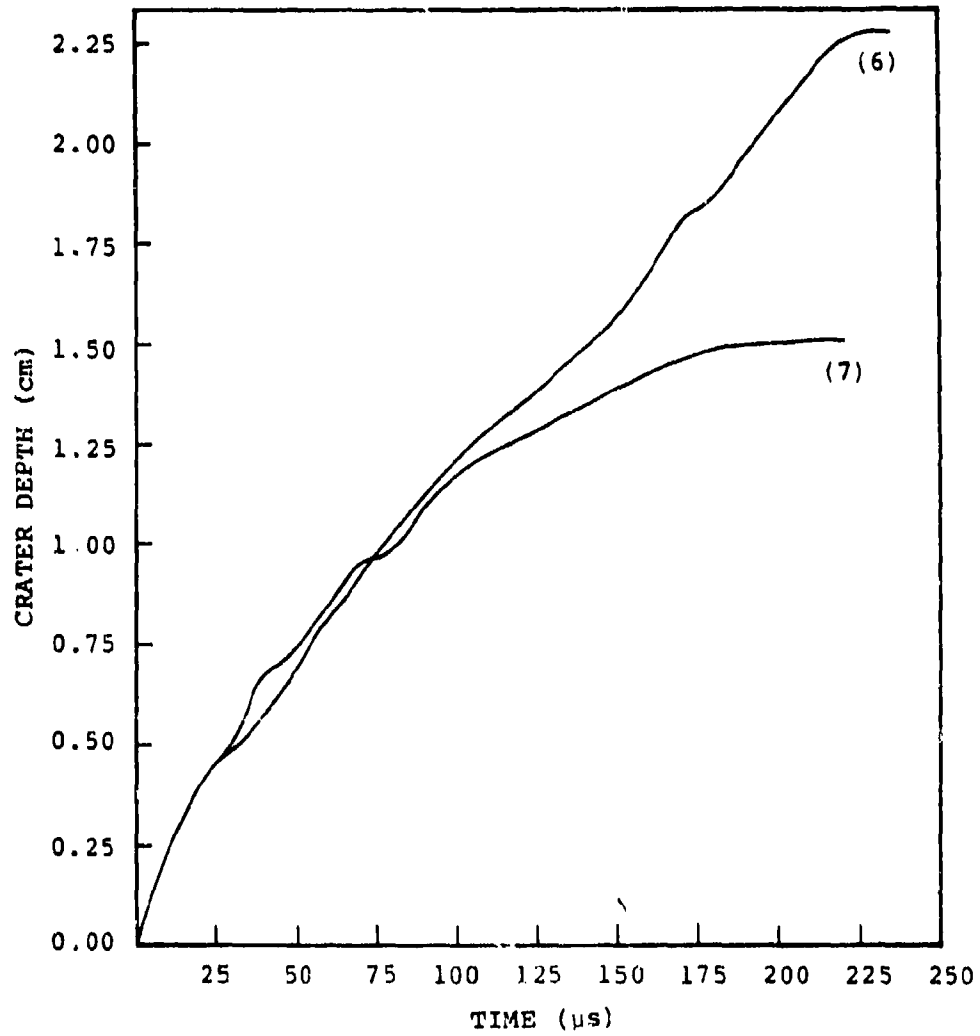


Figure 11. Crater Depth Versus Time for Calculations 6 and 7 (Soft Projectiles)

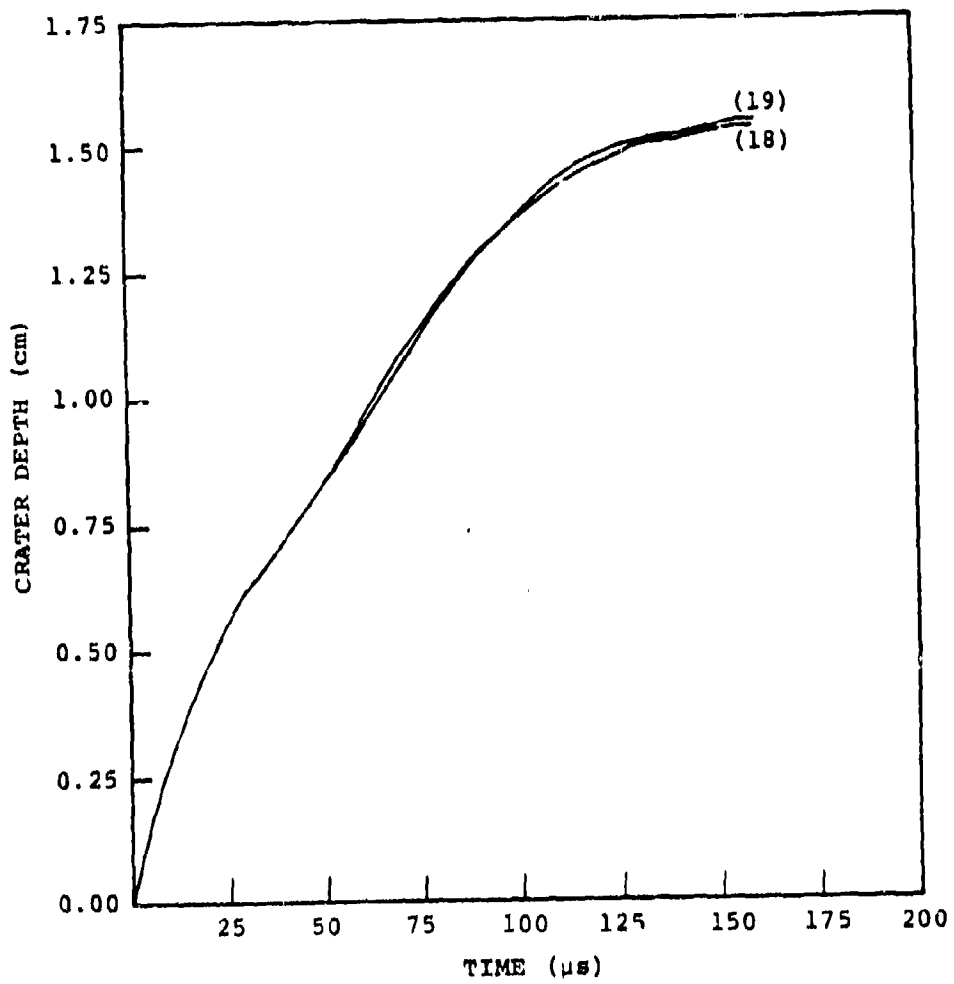


Figure 12. Crater Depth Versus Time for Calculations 18 and 19 (Hard Projectiles)

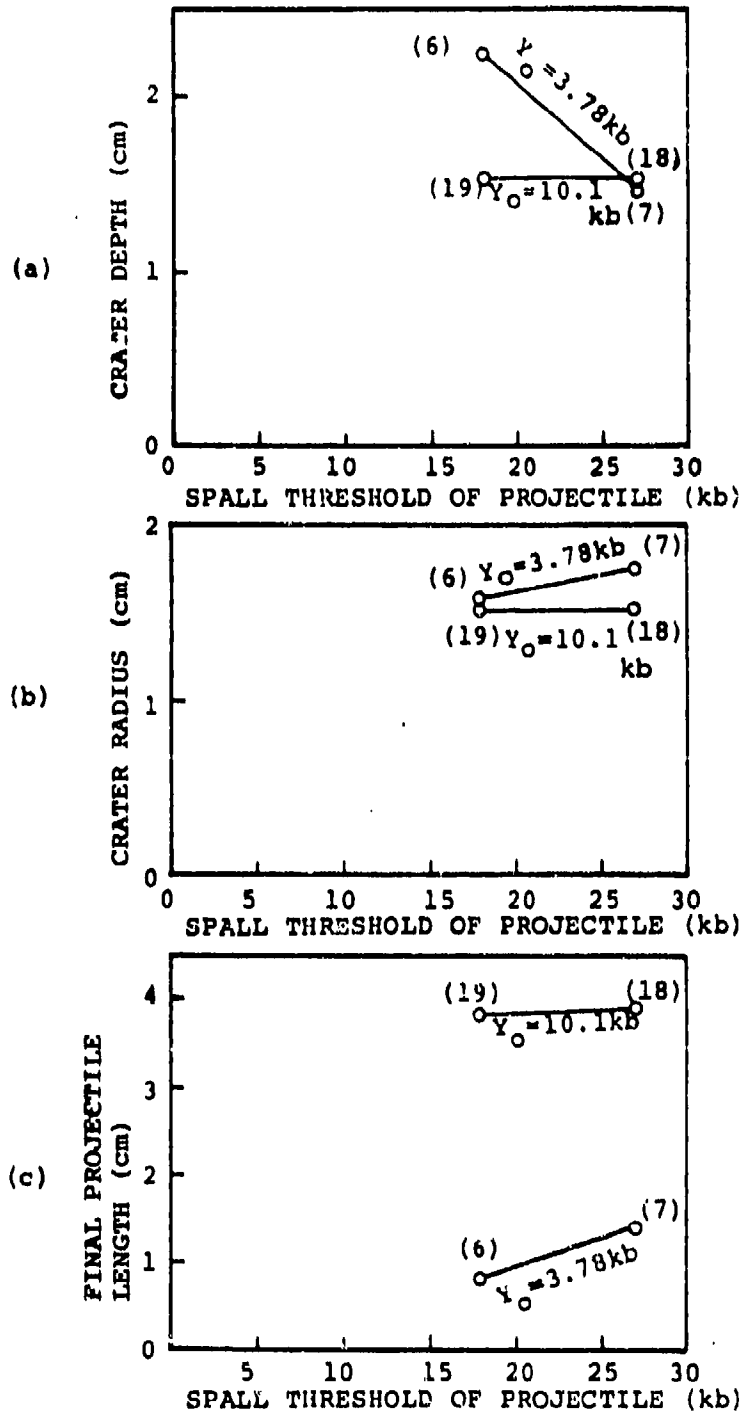


Figure 13. Final Crater Depth, Crater Radius, and Length of Projectile Versus Spall Threshold for Calculations 6, 7, 18, and 19

These results raise two interesting questions. (1) Why does decreasing the spall threshold of a soft projectile make it a better penetrator? (2) Why does decreasing the spall threshold of a hard projectile have no effect on its penetrability? It appears that the answers to both questions involve the effect of projectile shear yield strength on the penetration process.

In the first instance, the increased tensile failure in the projectile has two effects on the cratering process. It drastically reduces the plastic work of the projectile material, and it narrows down the area across which the projectile load is delivered. The first of these effects enables the projectile to couple more of its energy to the target, and the second enables it to form a deeper crater. Figures 14a and 14b show the effect of projectile spall threshold on the plastic work of the projectile and the total energy coupled to the target.

In the second instance, it can be concluded that the high strength of the hard projectile inhibits the radial flow of the material within the crater volume which, in turn, prevents hydrostatic tensions above 18 kilobars from occurring. This conclusion is supported by Figure 15 which compares the extent of failed material at 160 μ s for the calculations involving soft and hard projectiles, both having a spall threshold of 18 kilobars. In Figure 15 the shaded cells contain material which is expanded ($\rho < \rho_0$) and which at some point has failed. The calculations predict considerable failure of projectile material within the crater volume for the soft projectile (Calculation 6) and essentially none for the hard projectile (Calculation 19). It can be concluded, therefore, that the spall threshold for the hard projectile must be lower than 18 kilobars for it to affect the projectile's penetrability.

By comparing the crater depth curves versus time for Calculations 6 and 7 (Figure 11) and for Calculations 3, 4, 11, 12, and 13 (Figure 7), it is apparent that the yield strength of the projectile does affect the early stages of the cratering process, whereas the ductility of the projectile does not have a significant effect on the crater depth until after 100 μ s. These results seem to suggest that to optimize the performance of a heavy metal penetrator against a thick steel target it is important for it to have a high shear yield strength for the early stages of penetration and to have a low spall threshold for the late stages.

5.4 EFFECTS OF VARYING THE SHEAR MODULUS OF THE PROJECTILE

By comparing the results of Calculations 8, 14, 15, and 18, the effects of varying the projectile material shear

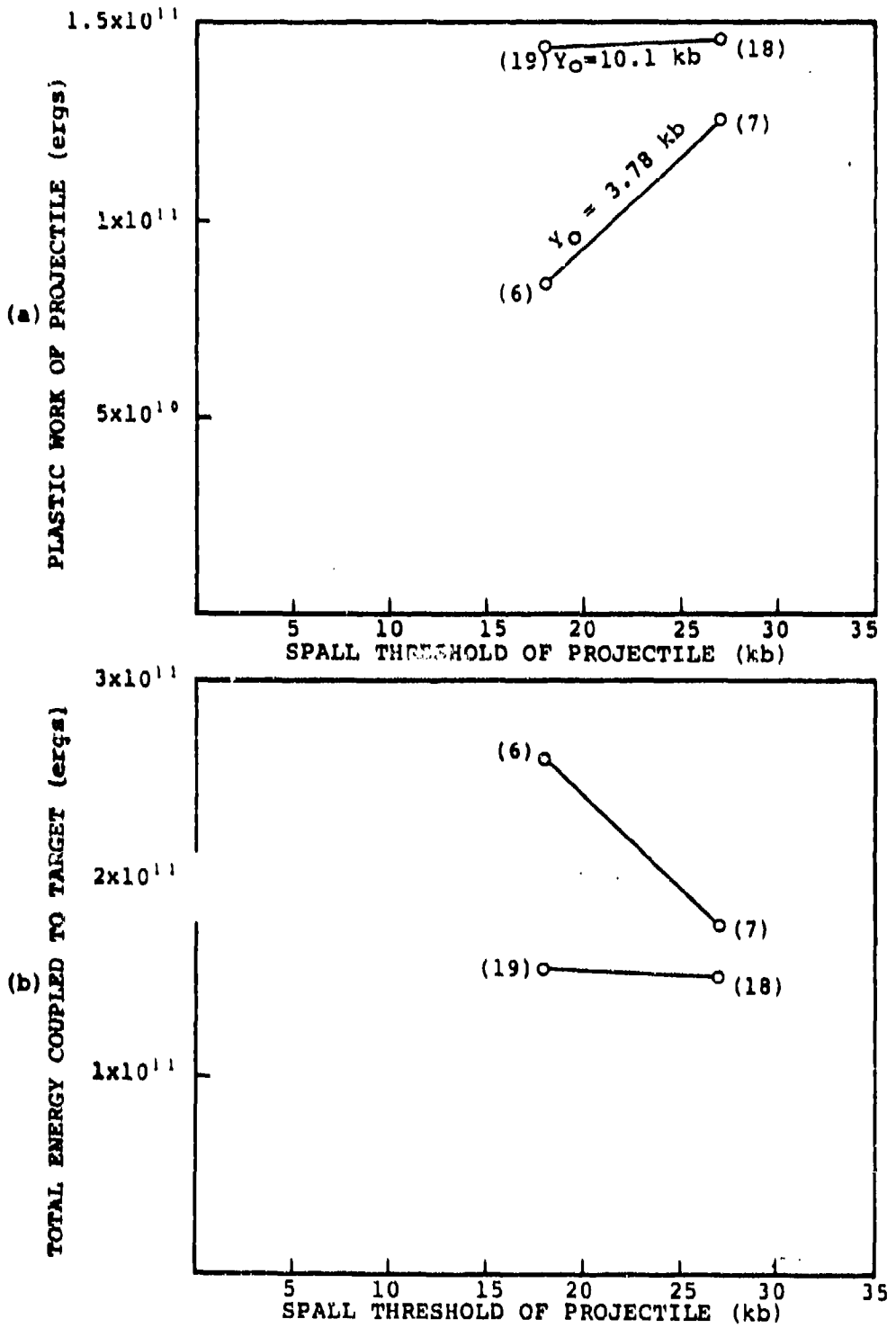
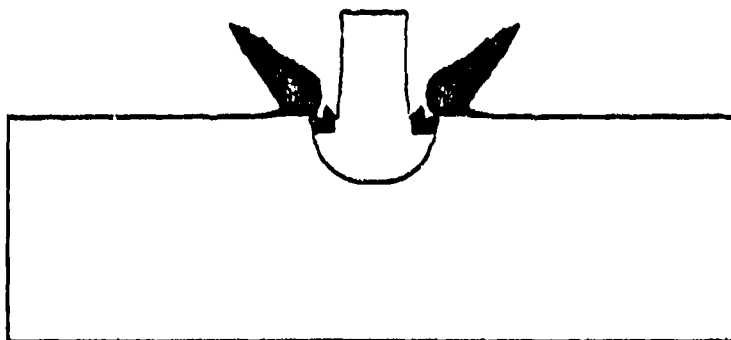


Figure 14a,b. Plastic Work of Projectile and Total Energy Coupled to the Target for Calculations 6, 7, 18, and 19

Calculation 19
 $Y_0 = 10.1 \text{ kb}$



Calculation 6
 $Y_0 = 3.78 \text{ kb}$

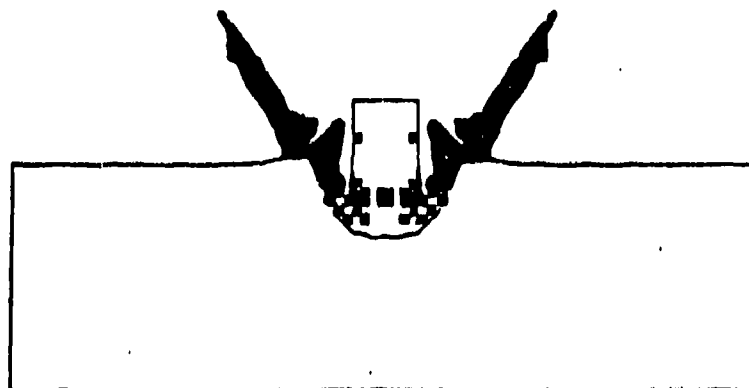


Figure 15. Configuration Plots of Calculations 6 and 19 at 160 μs . Failed Cells With Zero Stresses are Shaded. The Spall Threshold in Both Calculations was 18 Kilobars

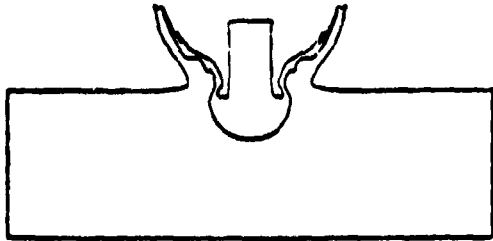
modulus can be observed. The shear modulus of a real heavy metal alloy, as modeled by Calculation 18, is 7.75×10^{11} dynes/cm². This value halved, i.e., 3.875×10^{11} dynes/cm², was used in Calculation 15, and in Calculations 8 and 14 the standard value was increased by factors of two and four to give shear moduli of 15.5×10^{11} dynes/cm² and 31.0×10^{11} dynes/cm², respectively. These four calculations therefore offer results over a substantial range of projectile shear moduli.

As the configuration plots in Figure 16 suggest, the final crater dimensions are rather insensitive to changes in the rigidity of the projectile. All of the craters are nearly hemispherical, and there is less than a 6 percent variation in the final crater depth or radius from the average values ($\bar{D} = 1.617$ cm, $\bar{R} = 1.514$ cm) predicted by these four calculations.

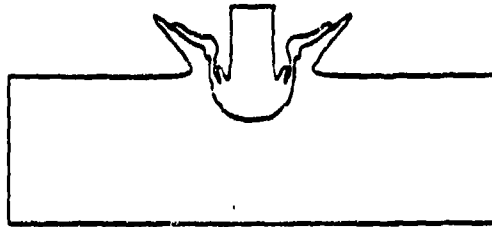
The final crater depths and radii are plotted versus projectile shear modulus in Figure 17a and 17b. Aside from the fact that there is some scatter in the crater depth data, a nearly horizontal line can be drawn through both the crater depth and crater radius data. Likewise, as indicated by Figure 17c, essentially the same total energy is coupled to the target during the cratering process by all four projectiles. Therefore, these results clearly predict a very weak relationship between projectile rigidity and penetrability.

The final length of the projectile, on the other hand, appears to increase significantly as the projectile shear modulus drops below 15.5×10^{11} dynes/cm², as seen in Figure 18a. It should be noted again, however, that the final projectile length is obtained at the time in the calculation that the final crater depth is established. As a result, these data points are an indication of how much of the projectile material is consumed in establishing a final crater depth, and they are not necessarily an indication of the projectile length when all of the projectile's kinetic energy has been dissipated. These calculations seem to indicate that while the back of the projectile is still moving toward the target, a significant amount of the projectile material flows radially and becomes part of the lip and debris before coming close enough to the projectile/target interface to affect the depth of the crater. In the plot of residual projectile kinetic energy versus projectile shear modulus in Figure 18b, it is evident that the projectiles with the lowest shear modulus have the largest residual kinetic energy as well as the greatest length when the crater depth is finalized. Consequently, at the time that the projectile kinetic energy goes to zero in Calculations 15 and 18, the

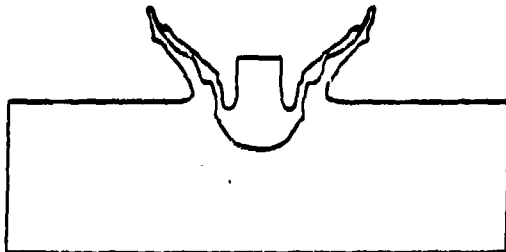
Calculation 15
 $G = 3.875 \times 10^{11}$ dynes/cm²



Calculation 18
 $G = 7.75 \times 10^{11}$ dynes/cm²



Calculation 8
 $G = 15.5 \times 10^{11}$ dynes/cm²



Calculation 14
 $G = 31.0 \times 10^{11}$ dynes/cm²

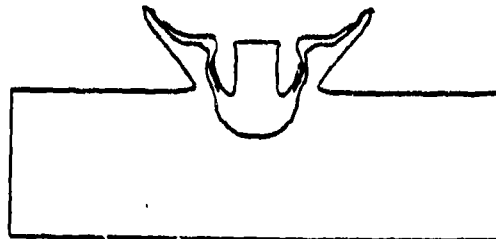


Figure 16. Final Configuration for Calculations 8, 14, 15, and 18

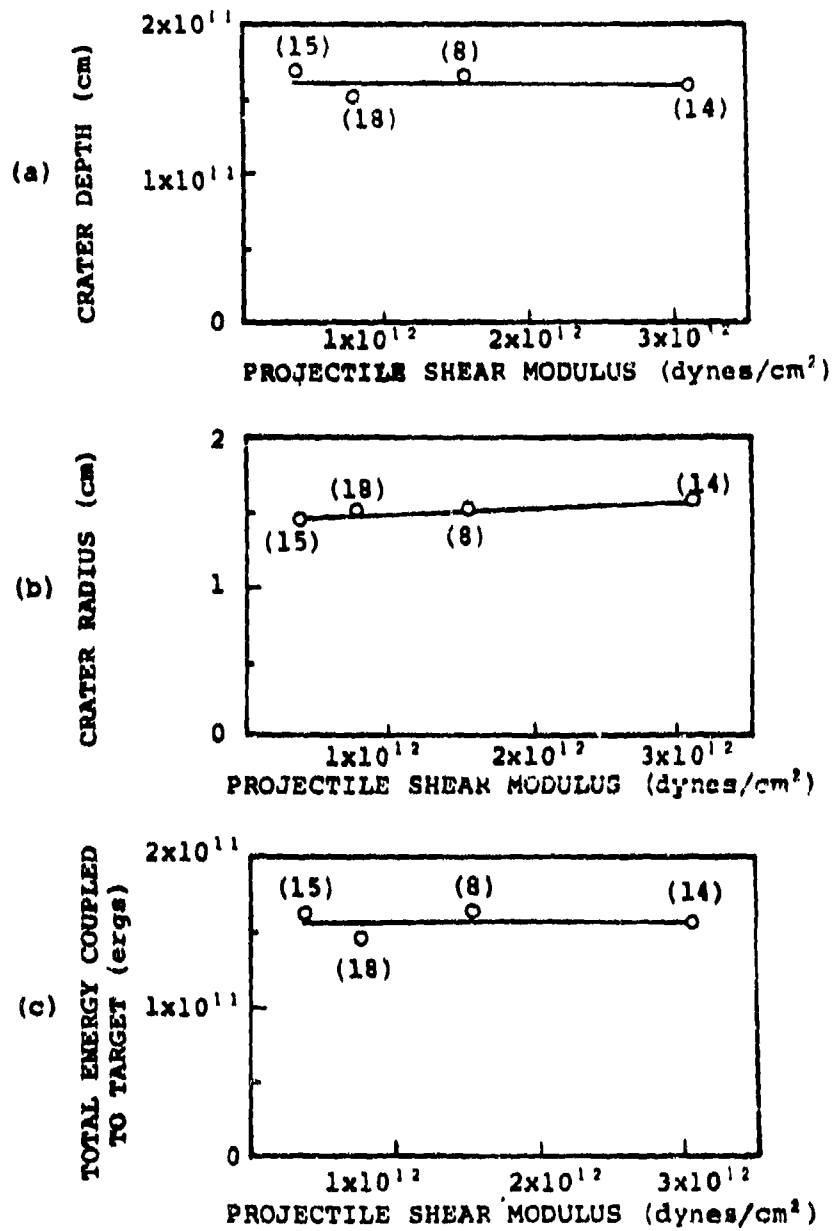


Figure 17. Crater Depth, Crater Radius, and Total Energy Coupled to the Target Versus Time for Calculations 8, 14, 15, and 16

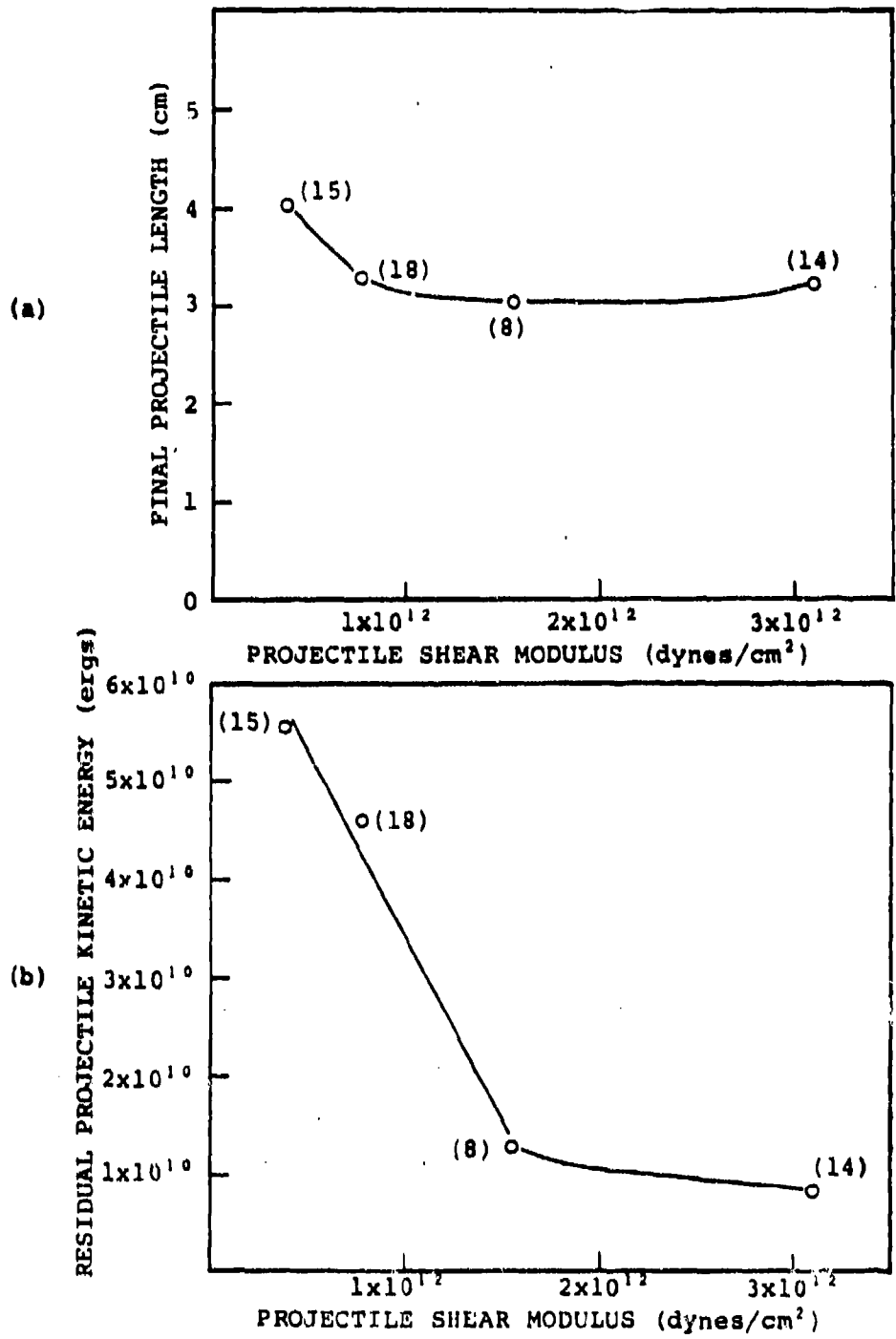


Figure 18. Final Projectile Length and Residual Projectile Kinetic Energy Versus Projectile Shear Modulus for Calculations 8, 14, 15, and 18

projectile length might be reduced to that of the projectiles in Calculations 8 and 14. Therefore, it is possible that the true final dimensions of the projectile as well as those of the crater are essentially unaffected by the rigidity of the projectile.

Finally, the similar shape and slope of the crater depth versus time curves in Figure 19 for Calculations 8, 14, 15, and 18 suggest that the growth rate of the crater is also essentially independent of the rigidity modulus of the projectile material.

5.5 EFFECTS OF VARYING THE BULK MODULUS OF THE PROJECTILE

Calculations 16, 17, and 18 were performed for the purpose of investigating the effects of varying the bulk modulus of the projectile material. In the standard calculation (18) the bulk modulus of a real heavy metal alloy, 1.095×10^{12} dynes/cm², was used. One-half of this value, or 5.975×10^{11} dynes/cm², was used in Calculation 16 and four times the standard value, or 4.38×10^{12} dynes/cm², was used in Calculation 17.

Figure 20 shows the predicted final projectile/target configurations for these three impact situations. It is evident from the projectile length and lip formation at crater arrest that the cratering process is somewhat affected by the bulk modulus of the projectile. However, the plots in Figure 21 show that the final dimensions of the crater and the energy coupled to the target are relatively insensitive to the bulk modulus of the projectile within the range represented here. It is apparent from the crater depth versus time curves in Figure 22 that the growth rates of the craters in these three calculations are not strongly affected by changes in the projectile bulk modulus. The curves remain coincident or parallel until 75 μ s, and they all begin to level off at about 125 μ s. Only the very late stages of the penetration, after 150 μ s, do their slopes significantly diverge.

As indicated in Table 4, the spall threshold, S , of the projectile in Calculations 16 and 17 was different from the 27-kilobar threshold used in Calculation 18. This difference arose from using the same value of $(\rho/\rho_0)_s$ for the projectile in the three calculations despite the change in the material bulk modulus, A . (Note from subsection 2.2.3, $(\rho/\rho_0)_s = \frac{S}{A} + 1$). The analysis of the effect of varying the projectile spall threshold in subsection 5.3 reveals, however, that when hard material projectiles are used, the cratering process and the final crater dimensions are essentially unaffected by a 50 percent increase in the spall threshold (from 18 to 27 kb).

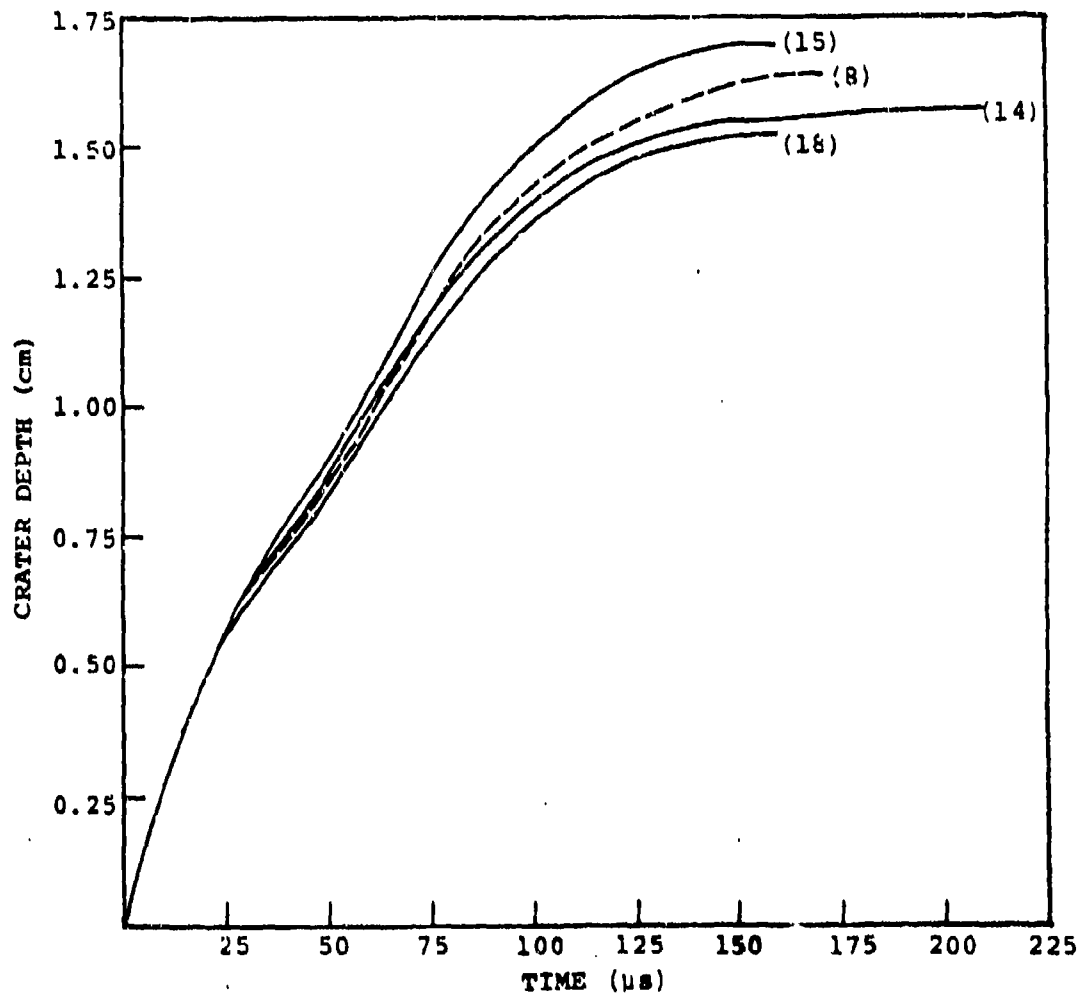
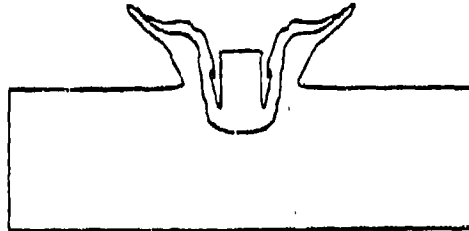
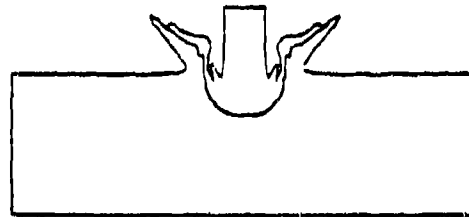


Figure 19. Crater Depth Versus Time for Calculations 8, 14, 15, and 18

Calculation 16
 $A = 5.975 \times 10^{11}$ dynes/cm²



Calculation 18
 $A = 1.095 \times 10^{12}$ dynes/cm²



Calculation 17
 $A = 4.38 \times 10^{12}$ dynes/cm²

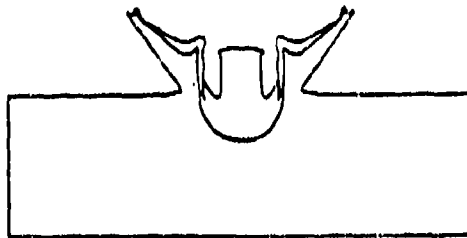


Figure 20. Predicted Final Configurations of Calculations 16, 17, and 18

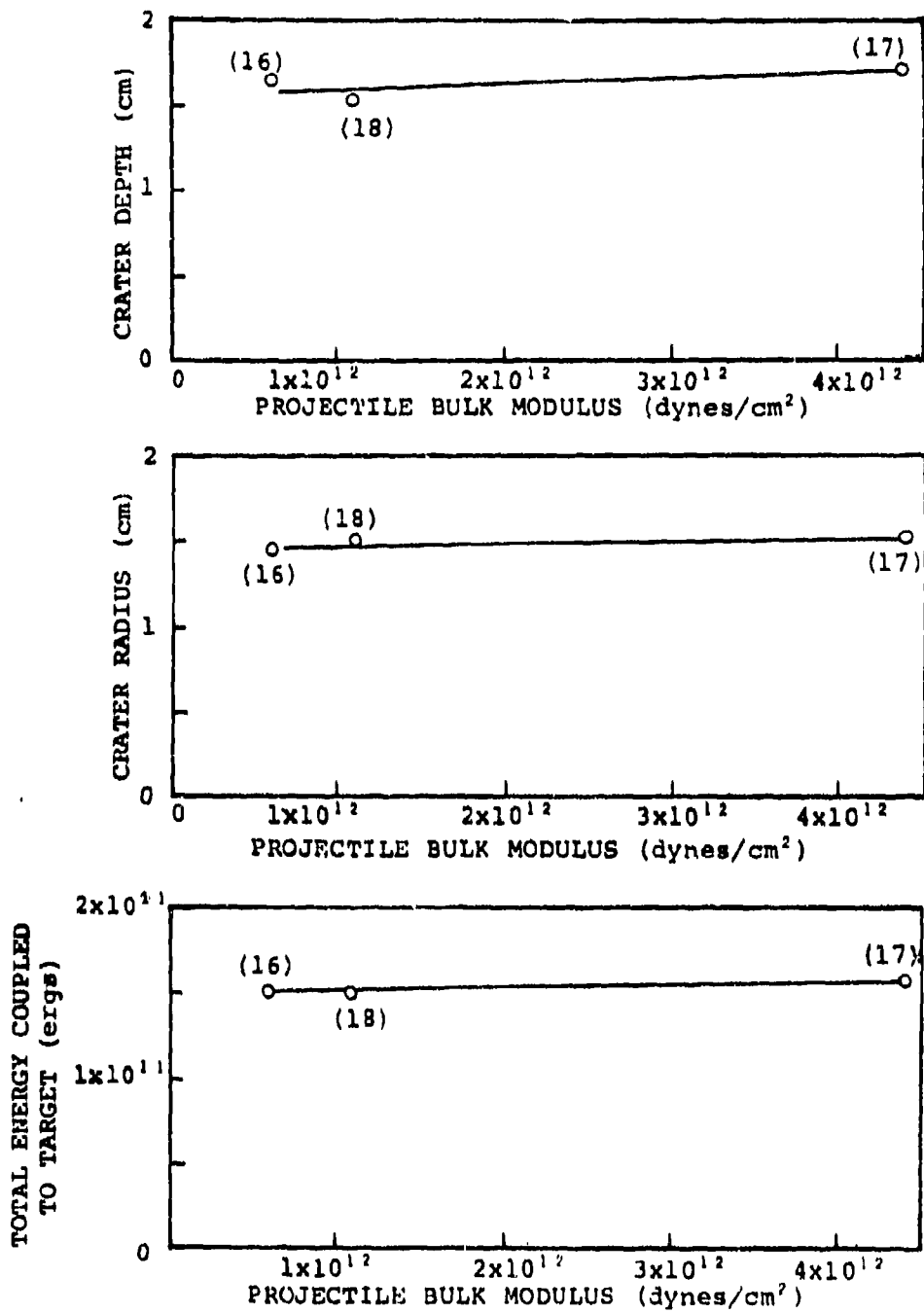


Figure 21. Crater Depth, Crater Radius, and Total Energy Coupled to Target for Calculations 16, 17, and 18

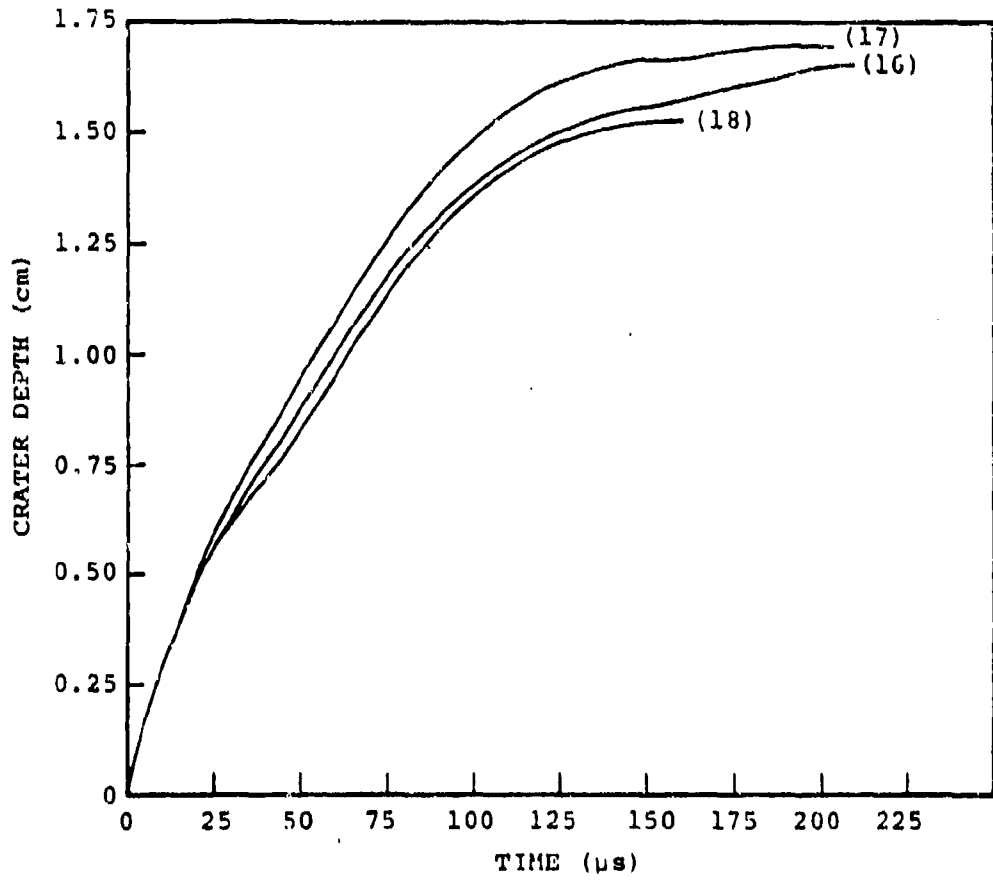


Figure 22. Crater Depth Versus Time for Calculations 16, 17, and 18

SECTION VI

CONCLUSIONS

In the current study the HELP code was employed to calculate eight impact situations to augment two earlier parametric investigations involving the effects of projectile material properties on penetration into a thick steel target. In all of the calculations heavy metal penetrators were impacted normally into a 5.08-cm-thick steel plate at a velocity of 5.5×10^4 cm/sec. The projectile material properties that were varied were the shear yield strength, the tensile failure threshold, the shear modulus, and the bulk modulus. Analysis of the results from the current calculational effort combined with the results from the two previous studies has led to the following conclusions. These conclusions apply to the particular impact situation studied.

- There exists a critical value of projectile material shear yield strength above which the crater depth is significantly increased by hardening the projectile material. Below this critical value, the crater depth is not strongly affected by increasing the shear yield strength of the projectile, and the trend is actually reversed when very soft ($Y_0 < 1.0$ kb) projectile materials are employed.
- Within the range of projectile material shear yield strengths considered in these studies ($0.75 \text{ kb} \leq Y_0 \leq 15.1 \text{ kb}$), the softer projectiles ($Y_0 \leq 2.55 \text{ kb}$) form wider craters and couple more total energy to the target than do the harder projectiles ($7.56 \text{ kb} \leq Y_0 \leq 15.1 \text{ kb}$).
- Since the crater depth resulting from an impact of a soft projectile ($Y_0 \leq 2.55 \text{ kb}$) is not established until nearly all of the projectile mass has been consumed by the penetration process, the initial dimensions of the projectile becomes an important parameter when the projectile material is relatively soft.
- Increasing the brittleness of a low yield strength projectile material ($Y_0 = 3.78 \text{ kb}$) by decreasing the tensile failure threshold from 27 to 18 kilobars results in a significantly deeper crater.

- Increasing the brittleness of a high yield strength projectile material ($Y_0 = 10.1 \text{ kb}$) by lowering the tensile failure threshold from 27 to 18 kilobars has essentially no effect on the crater dimensions. The 10.1-kilobar yield strength of the projectile material apparently prevents it from developing tensions that exceed the lower 1-kilobar failure threshold.
- The crater dimensions remain essentially the same when the shear modulus of the projectile material is increased an order of magnitude from $3.875 \times 10^{11} \text{ dynes/cm}^2$ to $3.1 \times 10^{12} \text{ dynes/cm}^2$.
- Changes in the bulk modulus of the projectile material between $5.975 \times 10^{11} \text{ dynes/cm}^2$ and $4.38 \times 10^{12} \text{ dynes/cm}^2$ do not strongly affect the final crater dimensions.

The results of these parametric studies indicate that the yield strength and the tensile failure threshold of a heavy metal penetrator strongly influence its ability to penetrate a thick steel target. However, a closer examination of the interdependence of the tensile failure threshold and the shear yield strength of the projectile material is required in order to optimize the effects of both characteristics. In particular, by employing numerical tools such as the HELP code, both material parameters can be varied in a series of calculations to find the optimum strength characteristics for a heavy metal penetrator.

Perhaps the most important extension of these parametric studies, however, should be the investigation of oblique impacts. Some of the above conclusions may very well be altered when the targets are impacted with significant degrees of obliquity. For example, brittleness of the projectile material, which seems to be an advantage in the normal impact situation studied here, may actually cause a long heavy metal penetrator to prematurely break in half when it impacts a target obliquely. Newly developed three-dimensional numerical techniques are available for the study of oblique impacts.

It is felt that finite difference numerical methods, when coordinated with experimental programs and when applied to parametric investigations such as the one reported here, can efficiently and economically provide valuable guidance to the designers of heavy metal penetrators.

REFERENCES

1. Sedgwick, R. T. and L. J. Walsh, "High Density Penetrator Performance in a Hard Target," AFATL-TR-74-201, ADB004857L, Air Force Armament Laboratory, Eglin Air Force Base, Florida, December 1974.
2. Hageman, L. J. and R. T. Sedgwick, "A Parametric Investigation of the Effects of Varying the Material Properties of a Heavy Metal Penetrator," AFATL-TR-75-152, Air Force Armament Laboratory, Eglin Air Force Base, Florida, November 1975.
3. Hageman, L. J. and J. M. Walsh, "HELP, A Multiple-Material Eulerian Program for Compressible Fluid and Elastic-Plastic Flows in the Two Space Dimensions and Time," I and II, BRL-CR-39, AD Nos. 726459 and 7626460, Ballistic Research Laboratories, Aberdeen Proving Ground, Maryland, May 1971.
4. Hageman, L. J., D. E. Wilkins, R. T. Sedgwick and J. L. Waddell, "HELP, A Multi-Material Eulerian Program for Compressible Fluid and Elastic-Plastic Flows in Two Space Dimensions and Time," Revised Edition, Systems, Science and Software Report SSS-R-75-2564, July 1975.
5. Tillotson, J. H., "Metallic Equations of State for Hypervelocity Impact," General Atomic Report GA-3216, July 1962.
6. Sedgwick, R. T. and L. J. Hageman, "Numerical, Analytical and Experimental Investigation of Penetration by Kinetic Kinetic Energy Projectiles," AFATL-TR-72-48, March 1972.
7. Sedgwick, R. T., M. S. Chawla and L. J. Walsh, "Parametric Application of Computer Codes to Metallic Projectile/Target Interactions," Systems, Science and Software Final Report SSS-R-73-1631 under Contract F08635-71-C-0094, April 1973.
8. Sedgwick, R. T., and J. M. Walsh, "Effects of Projectile Shape on Thin Plate Perforation at Normal Incidence," BRL-CR-38, May 1971.

APPENDIX A

PROJECTILE/TARGET CONFIGURATIONS AT VARIOUS TIMES FOR CALCULATIONS 1 THROUGH 19

In Figure A-1, the grid zoning employed in all of the HELP calculations is shown relative to the dimensions of the target and projectile. The remaining figures of this appendix give the predicted projectile/target configurations at various times for the nineteen HELP calculations used in the current analysis. In all cases calculational times of 5, 30, 60, 90, and 120 μ s and the final time corresponding to arrested crater growth are given. In each figure caption the spall threshold, S , shear yield strength, Y , bulk modulus Λ , and shear modulus, G are indicated in units of dynes/cm².

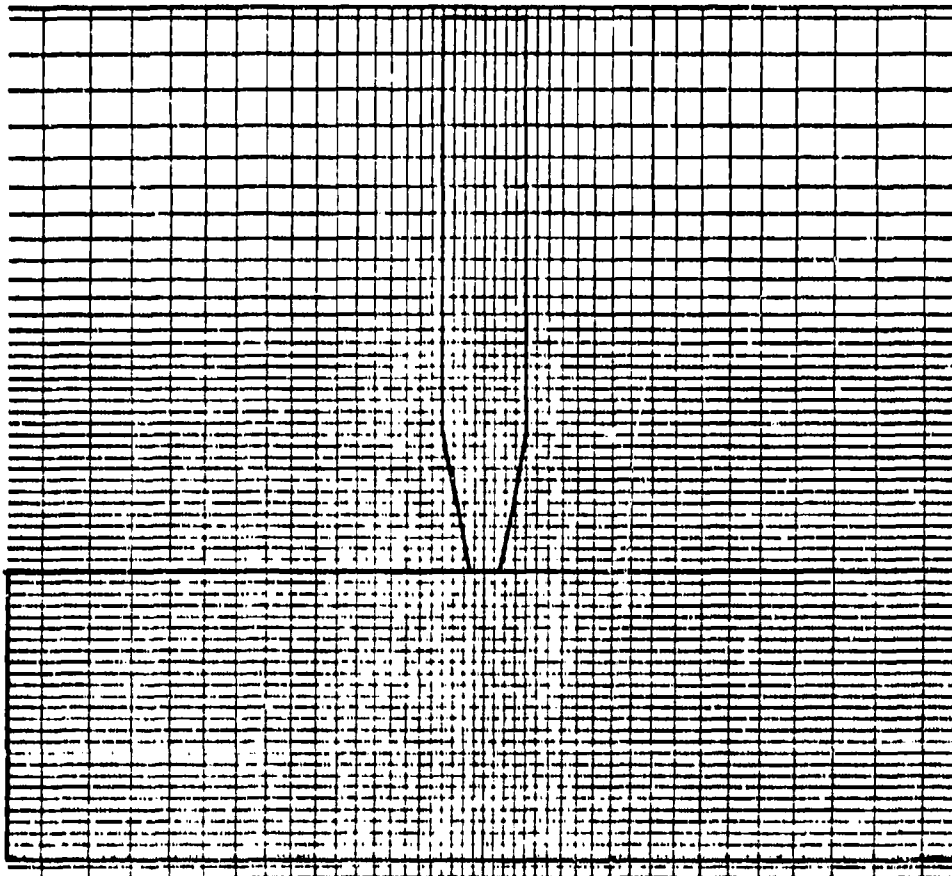
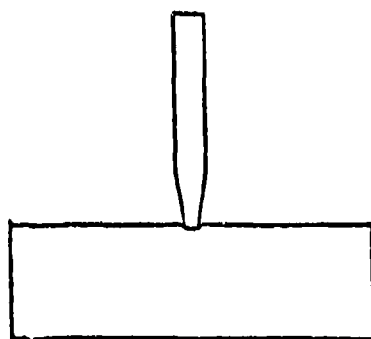
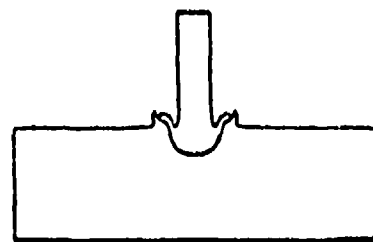


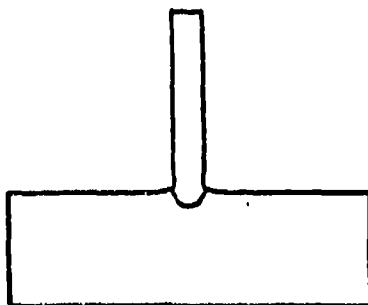
Figure A-1. Grid Zoning Employed in HELP Calculations. Only the Right Half of This Figure Represents the HELP Grid. The Code Uses Cylindrical Coordinates to Reflect the Axial Axis of Symmetry.



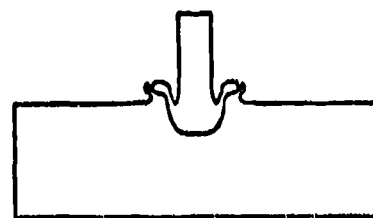
$t = 5 \mu s$



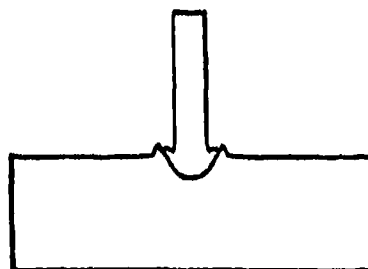
$t = 90 \mu s$



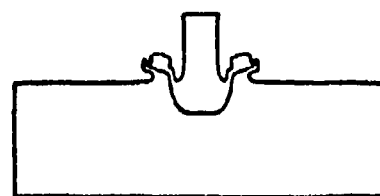
$t = 30 \mu s$



$t = 120 \mu s$

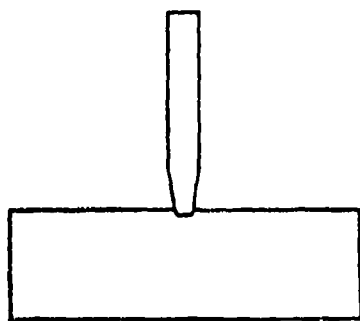


$t = 60 \mu s$

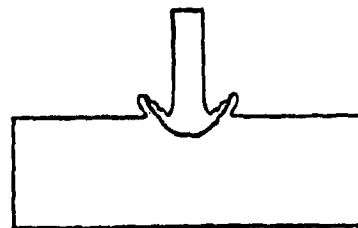


$t = 150 \mu s$

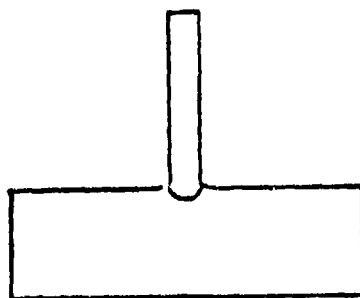
Figure A-2. Projectile/Target Configuration at Various Times for Calculation 1 ($S = 2.7 \times 10^{10}$, $Y_0 = 1.01 \times 10^{10}$, $G = 7.75 \times 10^{11}$, $A = 1.095 \times 10^{12}$)



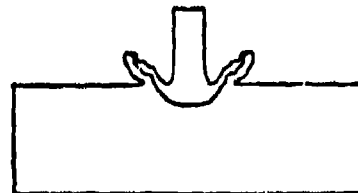
$t = 10 \mu s$



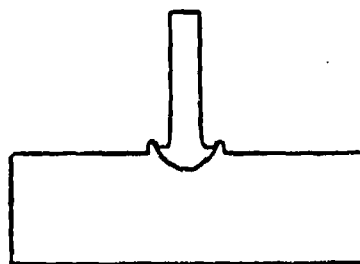
$t = 90 \mu s$



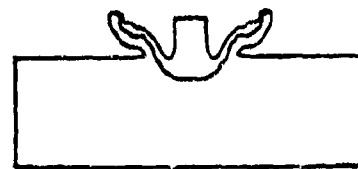
$t = 30 \mu s$



$t = 120 \mu s$

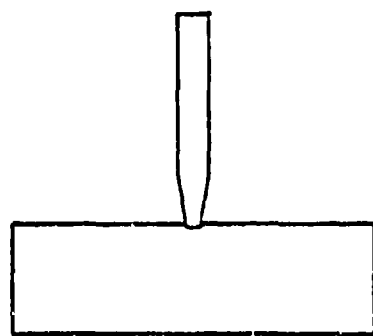


$t = 60 \mu s$

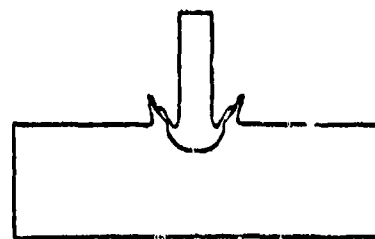


$t = 160 \mu s$

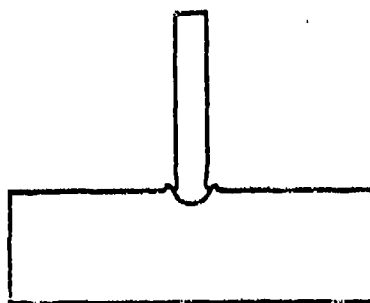
Figure A-3. Projectile/Target Configurations at Various Times for Calculation 2 ($S = 3.6 \times 10^{10}$, $Y_0 = 3.59 \times 10^9$, $G = 7.02 \times 10^{11}$, $A = 1.095 \times 10^{12}$)



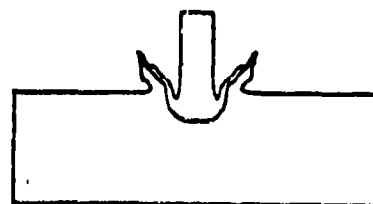
$t = 5 \mu s$



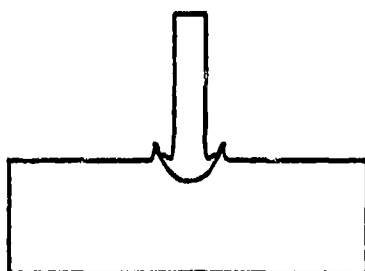
$t = 90 \mu s$



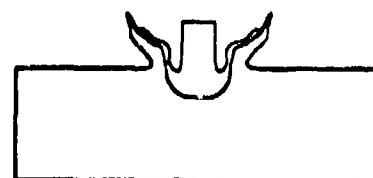
$t = 30 \mu s$



$t = 120 \mu s$

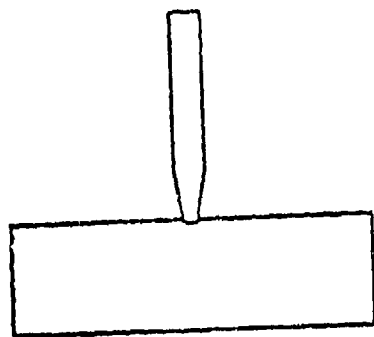


$t = 60 \mu s$

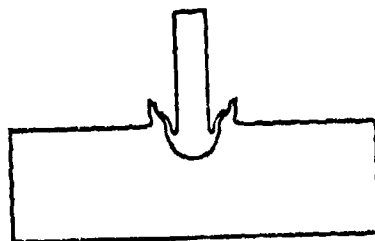


$t = 160 \mu s$

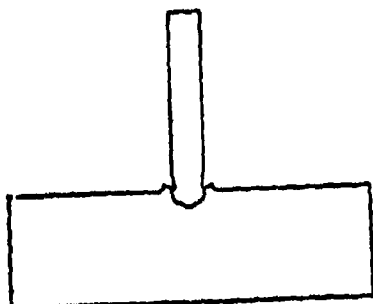
Figure A-4. Projectile/Target Configurations at Various Times for Calculation 3 ($S = 3.6 \times 10^{10}$, $Y_0 = 7.56 \times 10^9$, $G = 7.75 \times 10^{11}$, $A = 1.095 \times 10^{12}$)



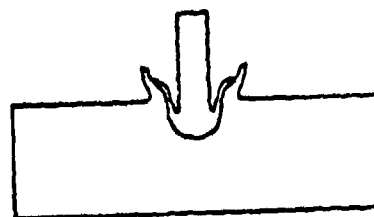
$t = 5 \mu s$



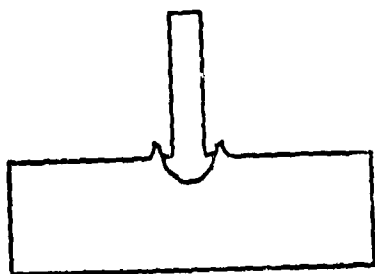
$t = 90 \mu s$



$t = 30 \mu s$



$t = 120 \mu s$

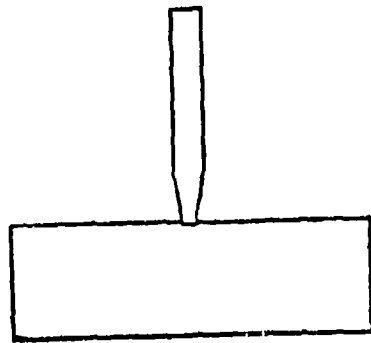


$t = 60 \mu s$

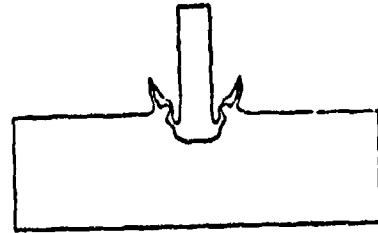


$t = 200 \mu s$

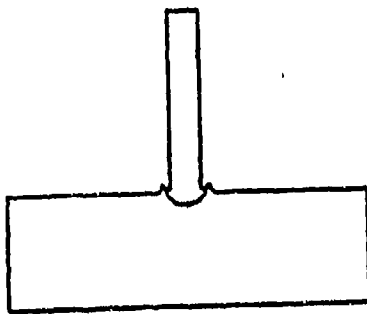
Figure A-5. Projectile/Target Configurations at Various Times for Calculation 4 ($S = 3.6 \times 10^{10}$, $Y_0 = 1.51 \times 10^{10}$, $G = 7.75 \times 10^{11}$, $A = 1.095 \times 10^{12}$)



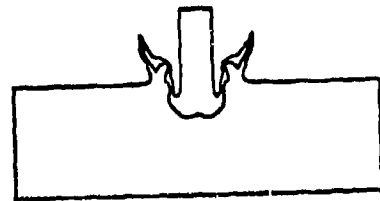
$t = 5 \mu s$



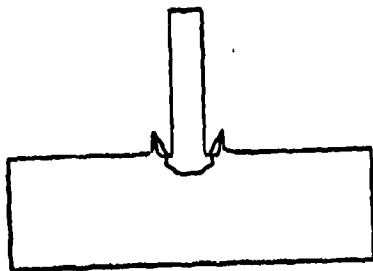
$t = 90 \mu s$



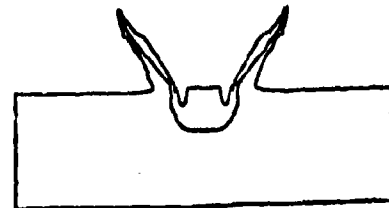
$t = 30 \mu s$



$t = 120 \mu s$

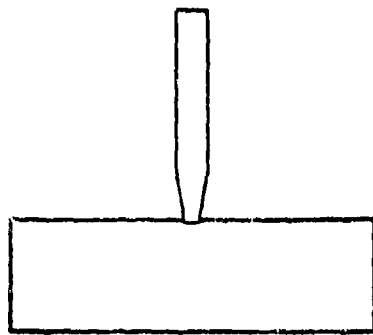


$t = 60 \mu s$

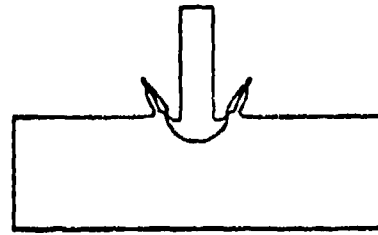


$t = 200 \mu s$

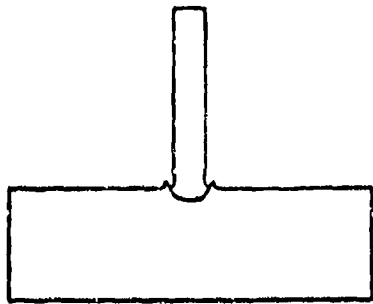
Figure A-6. Projectile/Target Configurations at Various Times for Calculation 5 ($S = 1.2 \times 10^{10}$, $Y_0 = 5.04 \times 10^9$, $G = 7.75 \times 10^{11}$, $A = 1.095 \times 10^{12}$)



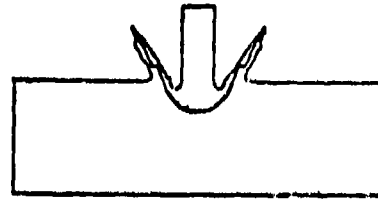
$t = 5 \mu s$



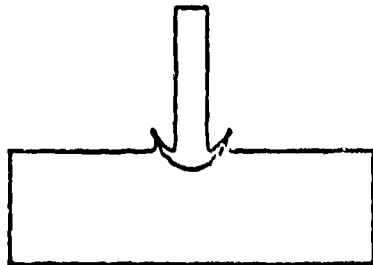
$t = 90 \mu s$



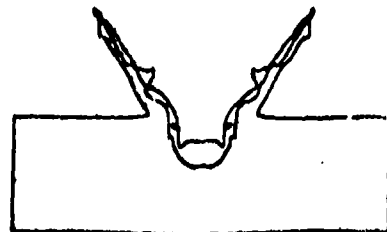
$t = 30 \mu s$



$t = 120 \mu s$

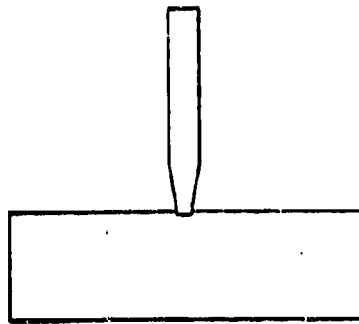


$t = 60 \mu s$

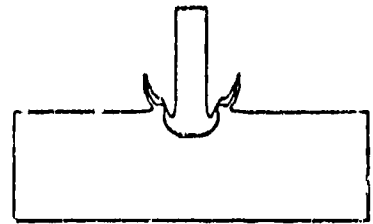


$t = 220 \mu s$

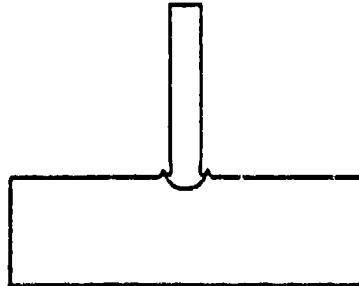
Figure A-7. Projectile/Target Configurations at Various Times for Calculation 6 ($S = 1.8 \times 10^{10}$, $Y_0 = 3.78 \times 10^9$, $G = 7.75 \times 10^{11}$, $A = 1.095 \times 10^{12}$)



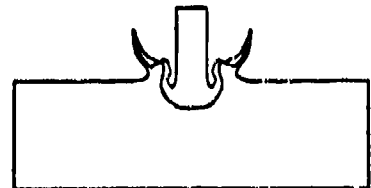
$t = 5 \mu s$



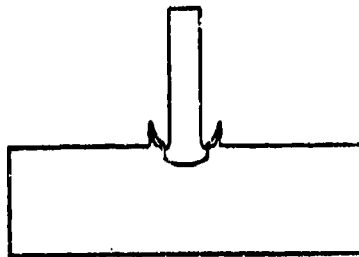
$t = 90 \mu s$



$t = 30 \mu s$



$t = 120 \mu s$

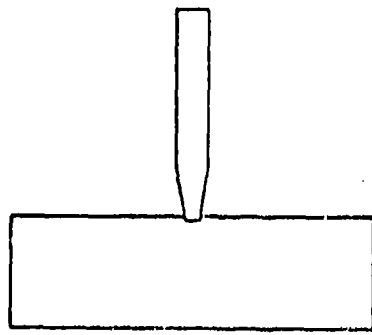


$t = 60 \mu s$

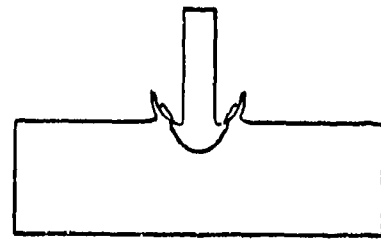


$t = 220 \mu s$

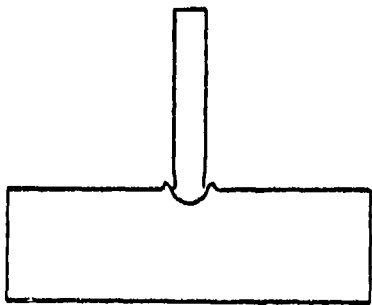
Figure A-8. Projectile/Target Configurations at Various Times for Calculation 7 ($S = 2.7 \times 10^{10}$, $Y_0 = 3.78 \times 10^9$, $G = 7.75 \times 10^{11}$, $A = 1.095 \times 10^{12}$)



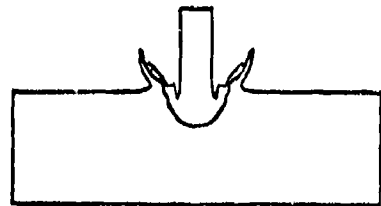
$t = 5 \mu s$



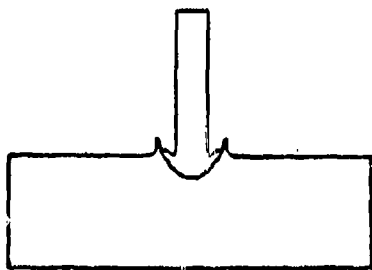
$t = 90 \mu s$



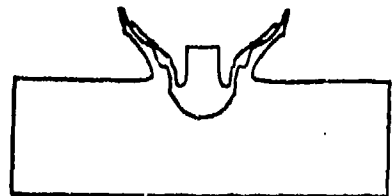
$t = 30 \mu s$



$t = 120 \mu s$

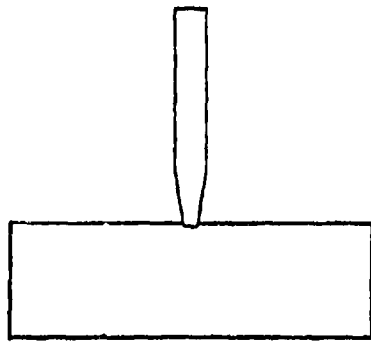


$t = 60 \mu s$

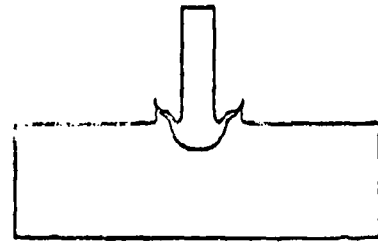


$t = 200 \mu s$

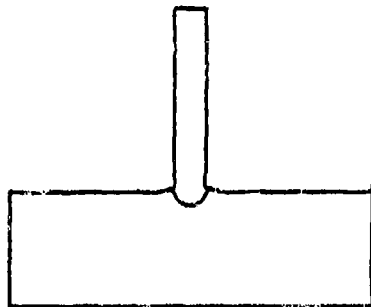
Figure A-9. Projectile/Target Configurations at Various Times for Calculation 8 ($S = 2.7 \times 10^{10}$, $Y_0 = 1.01 \times 10^{10}$, $G = 1.55 \times 10^{12}$, $A = 1.095 \times 10^{12}$)



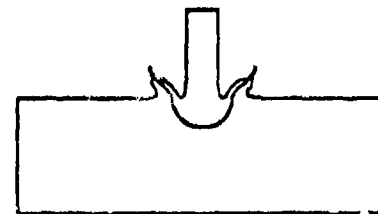
$t = 5 \mu s$



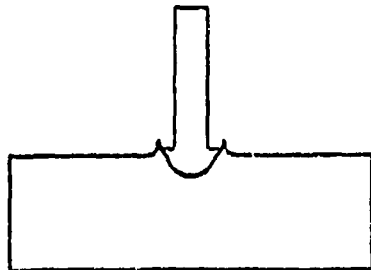
$t = 90 \mu s$



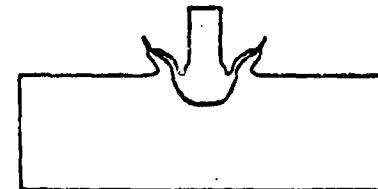
$t = 30 \mu s$



$t = 120 \mu s$



$t = 60 \mu s$



$t = 150 \mu s$

Figure A-10. Projectile/Target Configurations at Various Times for Calculation 9 ($S = 2.7 \times 10^{10}$, $\gamma_0 = 1.01 \times 10^{10}$, $G = 7.75 \times 10^{11}$, $A = 2.19 \times 10^{12}$)

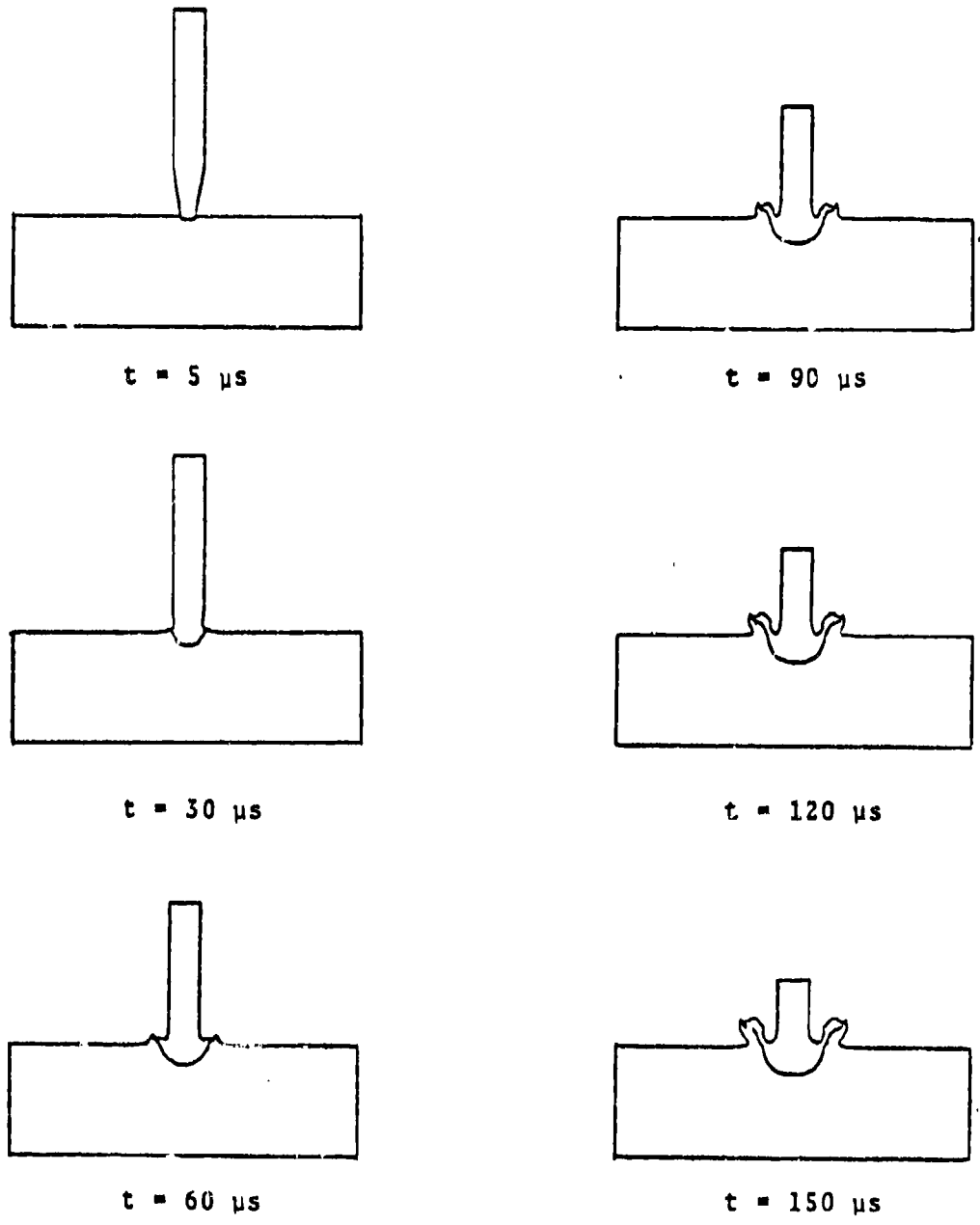
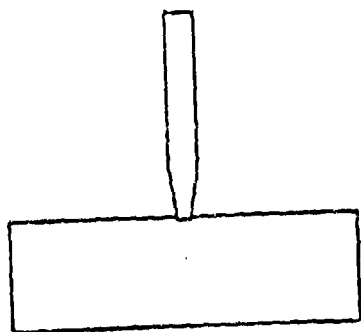
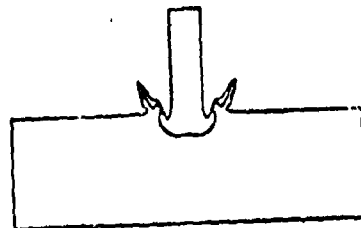


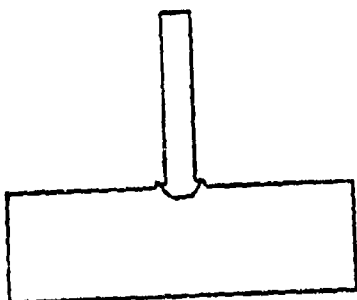
Figure A-11. Projectile/Target Configurations at Various Times for Calculation 10 ($S = 2.7 \times 10^{10}$, $Y_0 = 1.01 \times 10^{10}$, $G = 7.75 \times 10^{11}$, $A = 1.095 \times 10^{12}$, Abrupt Failure)



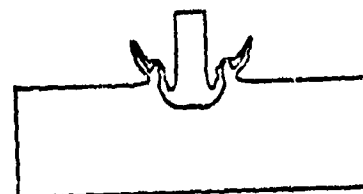
$t = 5 \mu s$



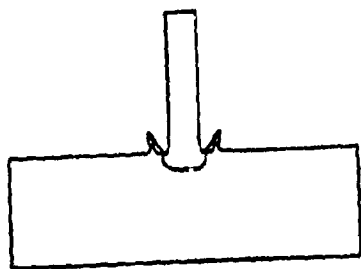
$t = 90 \mu s$



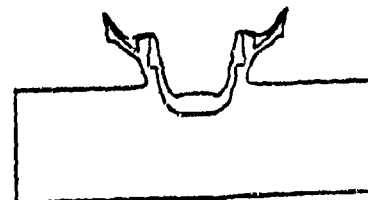
$t = 30 \mu s$



$t = 120 \mu s$



$t = 60 \mu s$



$t = 200 \mu s$

Figure A-12. Projectile/Target Configurations at Various Times for Calculation 11 ($S = 3.6 \times 10^{10}$, $Y_0 = 1.51 \times 10^9$, $G = 7.75 \times 10^{11}$, $A = 1.095 \times 10^{12}$)

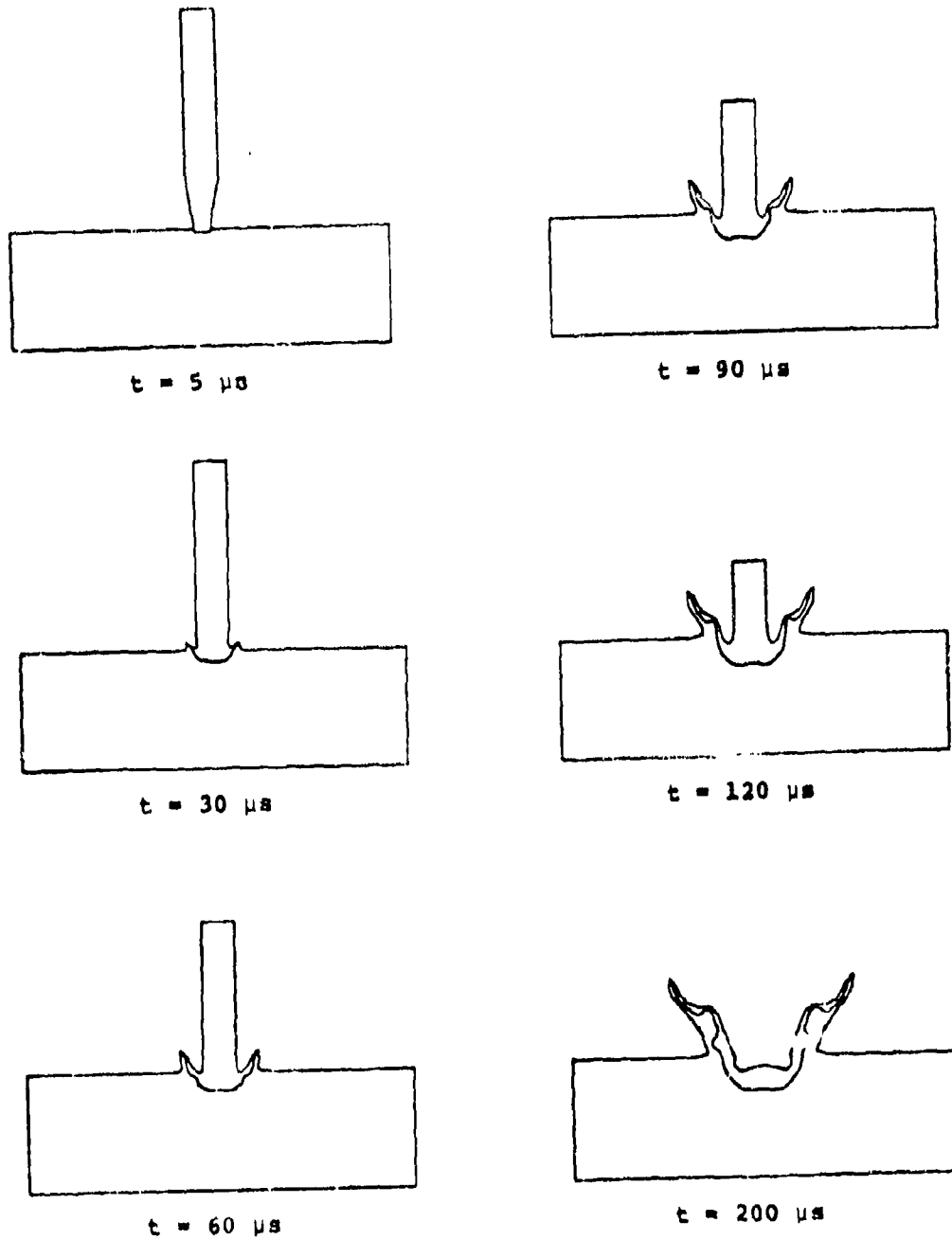
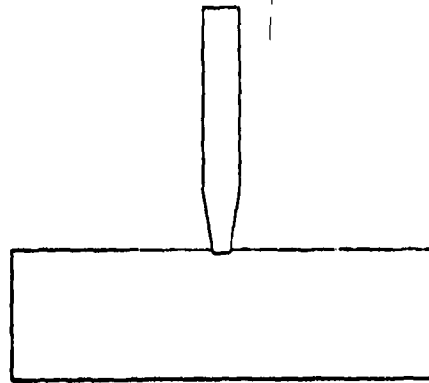
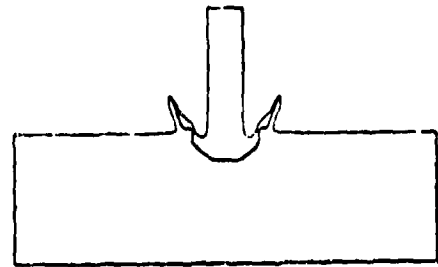


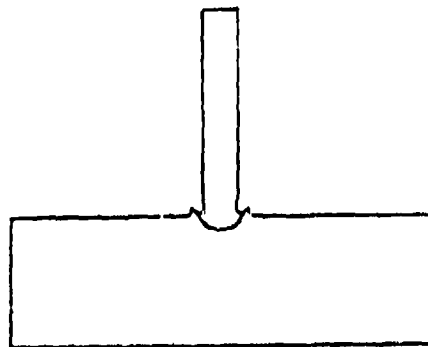
Figure A-13. Projectile/Target Configurations at Various Times for Calculation 12 ($S = 3.6 \times 10^{10}$, $Y_0 = 7.5 \times 10^8$, $G = 7.75 \times 10^{11}$, $A = 1.095 \times 10^{12}$)



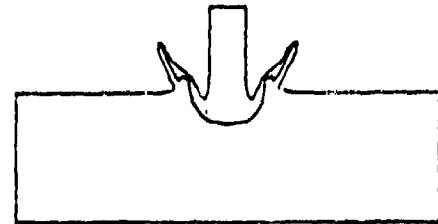
$t = 5 \mu s$



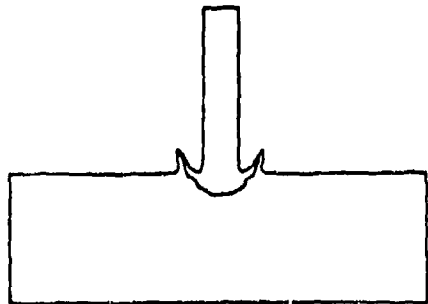
$t = 90 \mu s$



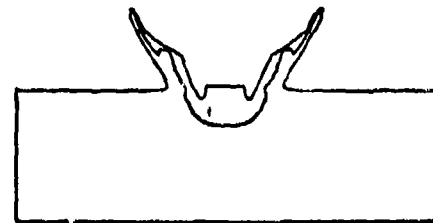
$t = 30 \mu s$



$t = 120 \mu s$



$t = 60 \mu s$



$t = 190 \mu s$

Figure A-14. Projectile/Target Configurations at Various Times for Calculation 13 ($S = 3.6 \times 10^{12}$, $Y_0 = 2.55 \times 10^9$, $G = 7.75 \times 10^{11}$, $A = 1.095 \times 10^{12}$)

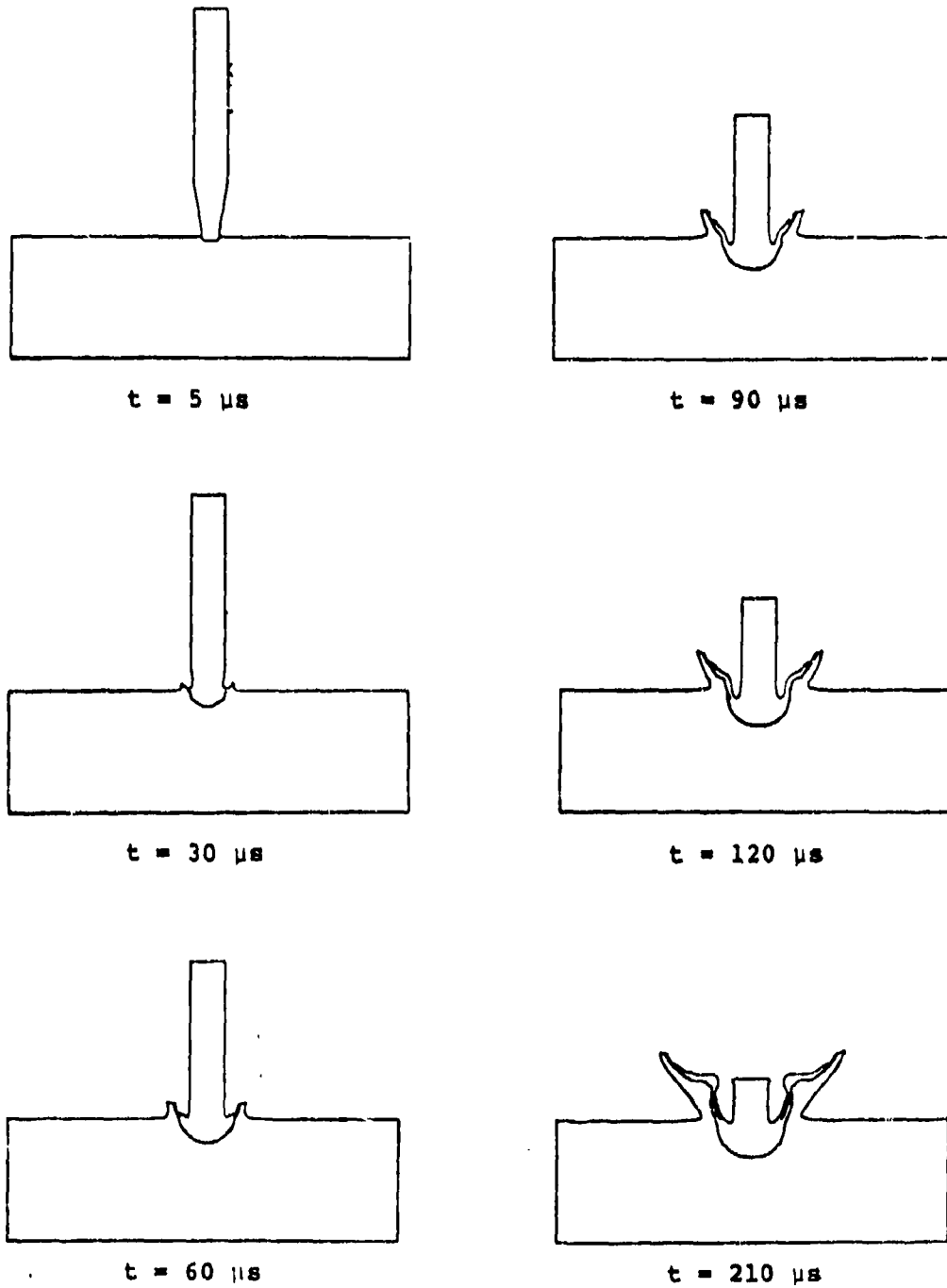
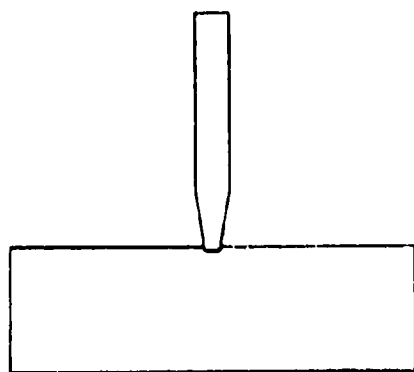
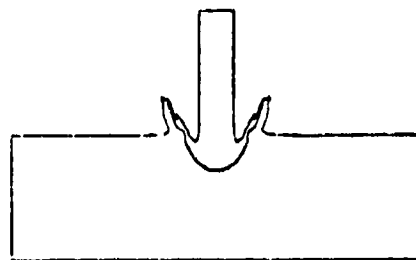


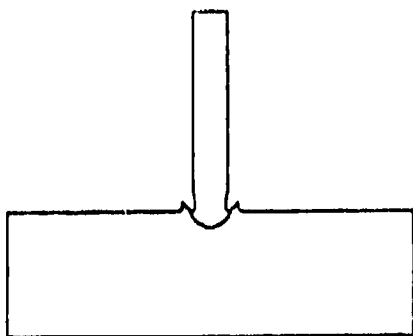
Figure A-15. Projectile/Target Configurations at Various Times for Calculation 14 ($S = 2.7 \times 10^{10}$, $Y_0 = 1.01 \times 10^{10}$, $G = 3.1 \times 10^{12}$, $A = 1.095 \times 10^{12}$)



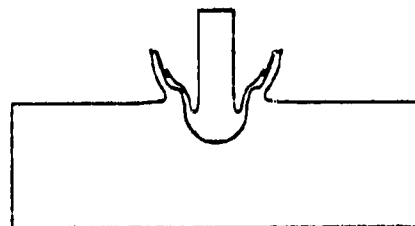
$t = 5 \mu s$



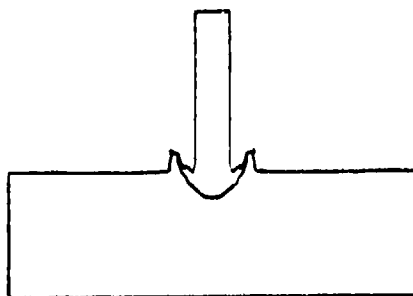
$t = 90 \mu s$



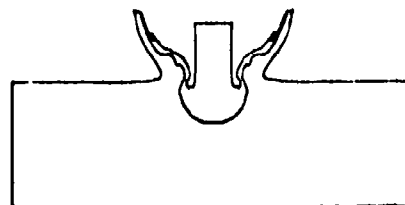
$t = 30 \mu s$



$t = 120 \mu s$

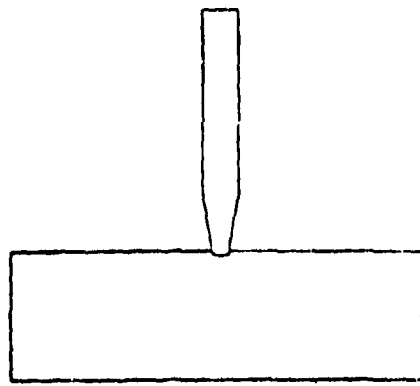


$t = 60 \mu s$

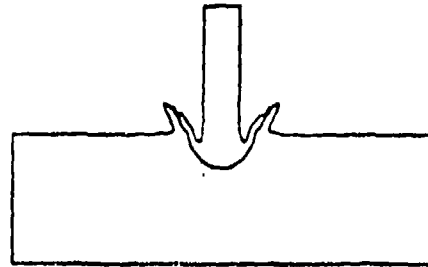


$t = 160 \mu s$

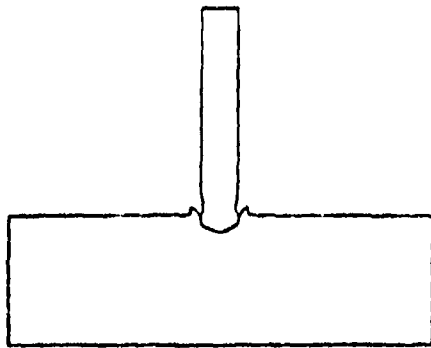
Figure A-16. Projectile/Target Configurations at Various Times for Calculation 15 ($S = 2.7 \times 10^{10}$, $Y_0 = 1.01 \times 10^{10}$, $G = 3.875 \times 10^{11}$, $A = 1.095 \times 10^{12}$)



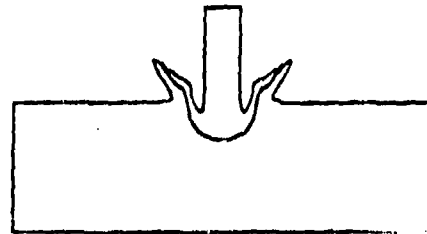
$t = 5 \mu s$



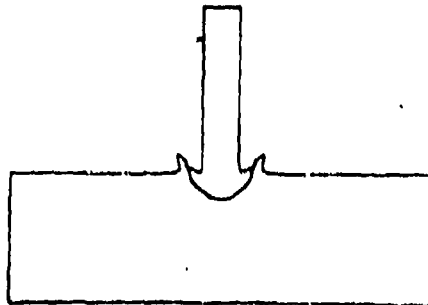
$t = 90 \mu s$



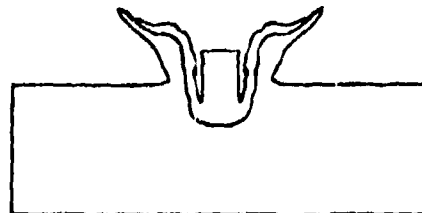
$t = 30 \mu s$



$t = 120 \mu s$



$t = 60 \mu s$



$t = 210 \mu s$

Figure A-17. Projectile/Target Configurations at Various Times for Calculation 16 ($S = 2.7 \times 10^9$, $Y_0 = 1.01 \times 10^{10}$, $G = 7.75 \times 10^{11}$, $\Lambda = 5.975 \times 10^{11}$)

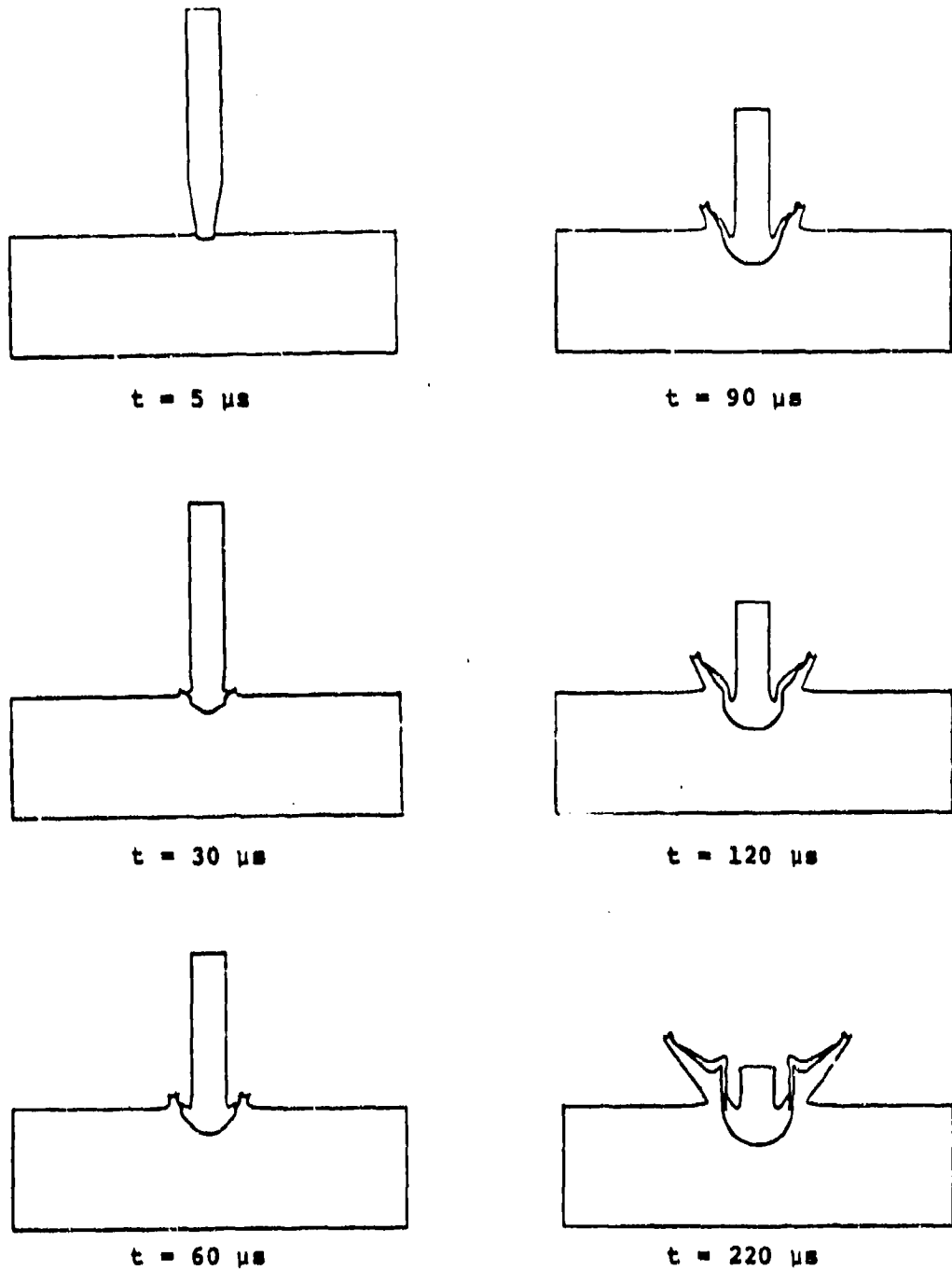
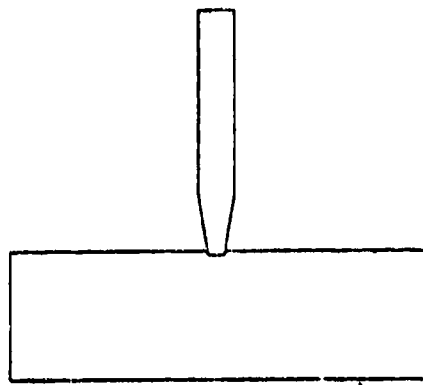
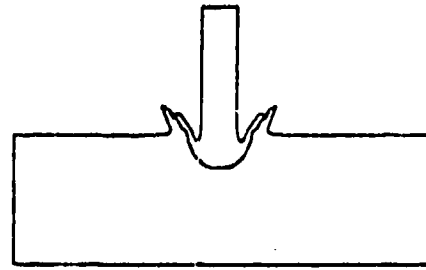


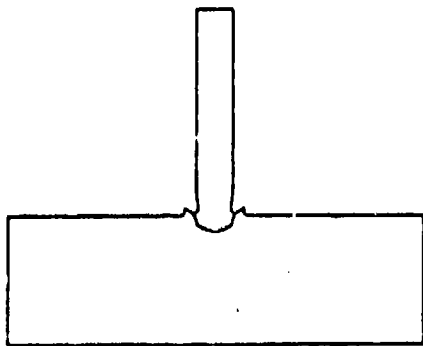
Figure A-18. Projectile/Target Configurations at Various Times for Calculation 17 ($S = 2.7 \times 10^{10}$, $Y_0 = 1.01 \times 10^{10}$, $G = 7.75 \times 10^{11}$, $A = 4.38 \times 10^{12}$)



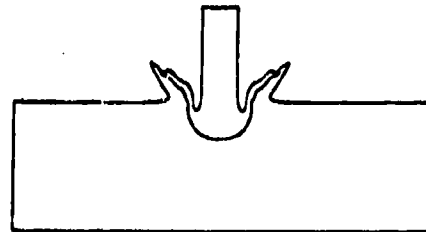
$t = 5 \mu s$



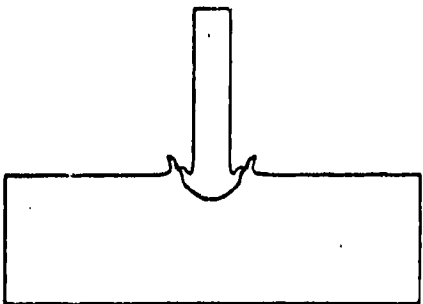
$t = 90 \mu s$



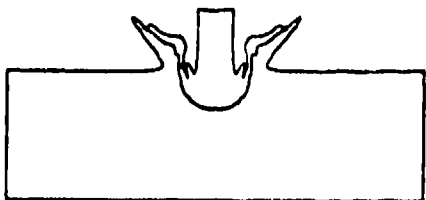
$t = 30 \mu s$



$t = 120 \mu s$

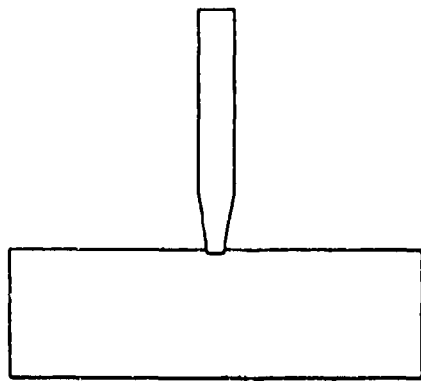


$t = 60 \mu s$

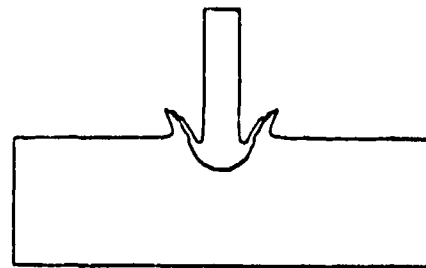


$t = 160 \mu s$

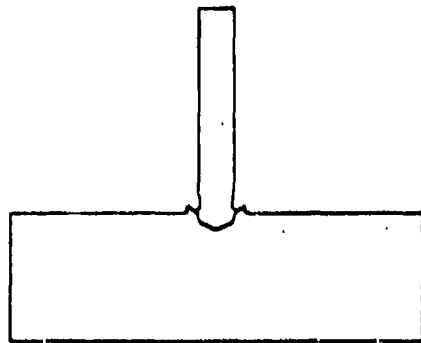
Figure A-19. Projectile/Target Configurations at Various Times for Calculation 18 ($S = 2.7 \times 10^{10}$, $Y_0 = 1.01 \times 10^{10}$, $G = 7.75 \times 10^{11}$, $A = 1.095 \times 10^{12}$)



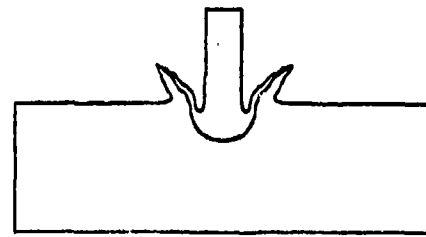
$t = 5 \mu s$



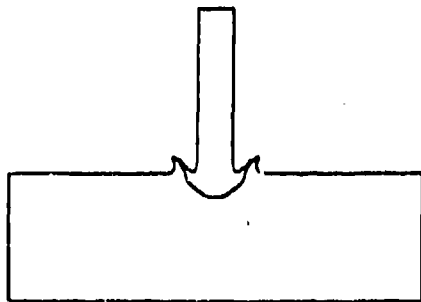
$t = 90 \mu s$



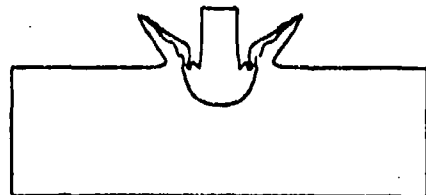
$t = 30 \mu s$



$t = 120 \mu s$



$t = 60 \mu s$



$t = 160 \mu s$

Figure A-20. Projectile/Target Configurations at Various Times for Calculation 19 ($S = 1.8 \times 10^{10}$, $Y_0 = 1.01 \times 10^{10}$, $G = 7.75 \times 10^{11}$, $A = 1.095 \times 10^{12}$)

INITIAL DISTRIBUTION

Hq USAF(AF/SAMI)	1
Hq AFSC/DLCAW	1
AFIT/LD	1
CIA-CRE/ADD/Pubs	2
AUL/AUL-LSE-70-239	1
Redstone Sci Info Cen/Doc Sec	2
Ballistic Res Labs	1
SARPA-TS	1
USN NAV ORD LAB/Tech Lib	2
NAV ORD STN/Tech Lib	1
NAV SYS Cen/Tech Lib 154	1
DDC/TC	2
Ogden ALC/MMNOP	2
US Atomic Energy Com/ Hq Lib	1
TAWC/TRADOCLO	1
AFATL/DL	1
AFATL/DLOSL	9
AFATL/DLDG	1
ASD/ENFEA	1
ASD/ENYEHM	1
AFIS/INTA	1
Systems, Science and Software	6
AF Materials Lab/MAMD	1
Georgia Inst of Technology	3
Lehigh University	1
University of Florida	2
AFATL/DLJW	10
AF Off of Sci Rsch/NAM	2
AEDC/ARO, Inc.	1
Hq TAC/DRA	1
Hq USAFE/DOQ	1
Hq PACAF/DOO	1
AFWL/LR	2